The Atlantic Water boundary current north of Svalbard in late summer

M. Dolores Pérez-Hernández[1] (ID)**, Robert S. Pickart[1]** (ID)**, Vladimir Pavlov[2], Kjetil Våge[3]** (ID)**, Randi Ingvaldsen[4]** (ID)**, Arild Sundfjord[2]** (ID)**, Angelika H. H. Renner[4], Daniel J. Torres[1]** (ID)**, and Svetlana Y. Erofeeva[5]**

[1]Department of Physical Oceanography, Woods Hole Oceanographic Institution, Woods Hole, Massachusetts, USA, [2]Norwegian Polar Institute, Tromsø, Norway, [3]Geophysical Institute, Bjerknes Centre for Climate Research, University of Bergen, Bergen, Norway, [4]Institute of Marine Research, Tromsø, Norway, [5]College of Oceanic and Atmospheric Sciences, Oregon State University, Corvallis, Oregon, USA

Abstract Data from a shipboard hydrographic/velocity survey carried out in September 2013 of the region north of Svalbard in the Nansen Basin are analyzed to characterize the Atlantic Water (AW) boundary current as it flows eastward along the continental slope. Eight meridional transects across the current, spanning an alongstream distance of 180 km, allow for a detailed description of the current and the regional water masses. During the survey the winds were light and there was no pack-ice. The mean section reveals that the boundary current was O(40 km) wide, surface-intensified, with a maximum velocity of 20 cm/s. Its mean transport during the survey was 3.11 ± 0.33 Sv, of which 2.31 ± 0.29 Sv was AW. This suggests that the two branches of AW entering the Arctic Ocean via Fram Strait—the Yermak Plateau branch and the Svalbard branch—have largely combined into a single current by 30°E. At this location the boundary current meanders with a systematic change in its kinematic structure during offshore excursions. A potential vorticity analysis indicates that the flow is baroclinically unstable, consistent with previous observations of AW anticyclones offshore of the current as well as the presence of a near-field cyclone in this data set. Our survey indicates that only a small portion of the boundary current is diverted into the Kvitøya Trough (0.17 ± 0.08 Sv) and that the AW temperature/salinity signal is quickly eroded within the trough.

Plain Language Summary From 15-28 September 2013 the R/V Lance carried out an oceanographic cruise to characterize the inflow of Atlantic Water (AW) north of Svalbard (80-83° N and 18-34° E). During the survey the winds were light and there was no pack-ice. The inflow of AW is observed as a warm and salty layer nearly 40 km wide, flowing eastward in the depth range 75-500m. The current generally flows parallel to the shelf-break, but it meanders and is able to generate eddies. Even though two distinct currents transporting AW emerge from Fram Strait into the Arctic Ocean (the Yermak and Svalbard branches), at our study area they appear as a single, combined flow. A small portion of this boundary current enters in the Kvitøya Trough, but its warm and salty signature is quickly eroded.

1. Introduction

One of the major circulation components of the Arctic Ocean is the Atlantic Water (AW) boundary current, which transports heat and salt throughout both the Eurasian and Canadian Basins [*Rudels et al.*, 2015; *Aksenov et al.*, 2016]. Part of the AW contributes to the structure and stability of the Arctic halocline [*Schauer et al.*, 2002; *Rudels et al.*, 2004; *Polyakov et al.*, 2011]. The remaining portion in the boundary current is significantly transformed and, as such, contributes to the global meridional overturning circulation. *Rudels et al.* [2015] concluded that of the 3.7 Sv of upper layer water that exit the Arctic Ocean, 2.9 Sv are supplied by the Atlantic inflow, most of which flows through Fram Strait. Historically, the AW boundary current has been thought of as a system of cyclonically flowing currents at the margins of the basins [*Coachman and Barnes*, 1963; *Rudels et al.*, 1994; *Aagaard and Carmack*, 1994]. The analyses of more recently collected data, including shipboard observations [e.g., *Schauer et al.*, 2002] and mooring deployments [e.g., *Polyakov et al.*, 2005], have enhanced our understanding of the AW pattern in the Arctic and confirmed this general view of the boundary current system [e.g., *Aksenov et al.*, 2016].

AW enters the Arctic Ocean through Fram Strait and through St. Anna Trough via the Barents Sea (Figure 1). To date, the exchange through the former has been studied more extensively [*Fahrbach et al.*, 2001; *Schauer and Beszczynska-Möller*, 2009; *Beszczynska-Möller et al.*, 2012]. The main northward conduit of AW in Fram Strait is the West Spitsbergen Current which on average transports about 3 ± 0.2 Sv of water warmer than 2°C into the Arctic Basin [*Beszczynska-Möller et al.*, 2012] (Figure 1). Near 79°N, the current divides into three distinct branches [*Perkin and Lewis*, 1984] that distribute AW as follows: a western branch that recirculates 1.6 Sv in the vicinity of the strait [*Håvik et al.*, 2017], an offshore branch transporting 1.7 ± 0.1 Sv, part of which progresses around the Yermak Plateau, and the Svalbard branch that flows along the continental slope of Svalbard carrying 1.3 ± 0.1 Sv [*Beszczynska-Möller et al.*, 2012] (Figure 1). It is not clear how or where (or even if) the Yermak and the Svalbard branches merge again, but, as suggested by *Perkin and Lewis* [1984], both branches seem to be present to the east of the Yermak Plateau flowing roughly along the continental shelfbreak [*Rudels et al.*, 2000, 2015] (Figure 1).

Overall, relatively little is known about the AW boundary current downstream of Fram Strait. Synoptic sections have shed light on the structure of the current [*Cokelet et al.*, 2008; *Schauer et al.*, 2002; *Pnyushkov et al.*, 2015; *Schauer et al.*, 1997], but there are very few transport estimates due to the dearth of shipboard velocity measurements and limited mooring observations. Using a single mooring upstream of the Lomonosov Ridge (guided by hydrographic data), *Woodgate et al.* [2001] estimated that the transport of the current over a year was approximately 5 Sv. Based on two sections of absolute geostrophic velocity across the current (separated by only a few hours) near 30°E, the AW transport was estimated to be 1.6 ± 0.3 Sv [*Våge et al.*, 2016]. Other synoptic estimates indicate that the AW transported by the Svalbard branch is approximately 2 Sv [*Schauer et al.*, 2004; *Beszczynska-Möller et al.*, 2011].

Mooring measurements have, however, offered insights into the seasonality of the AW boundary current. *Randelhoff and Sundfjord* [2015] described the seasonal variability in the upper layer temperatures in fall/
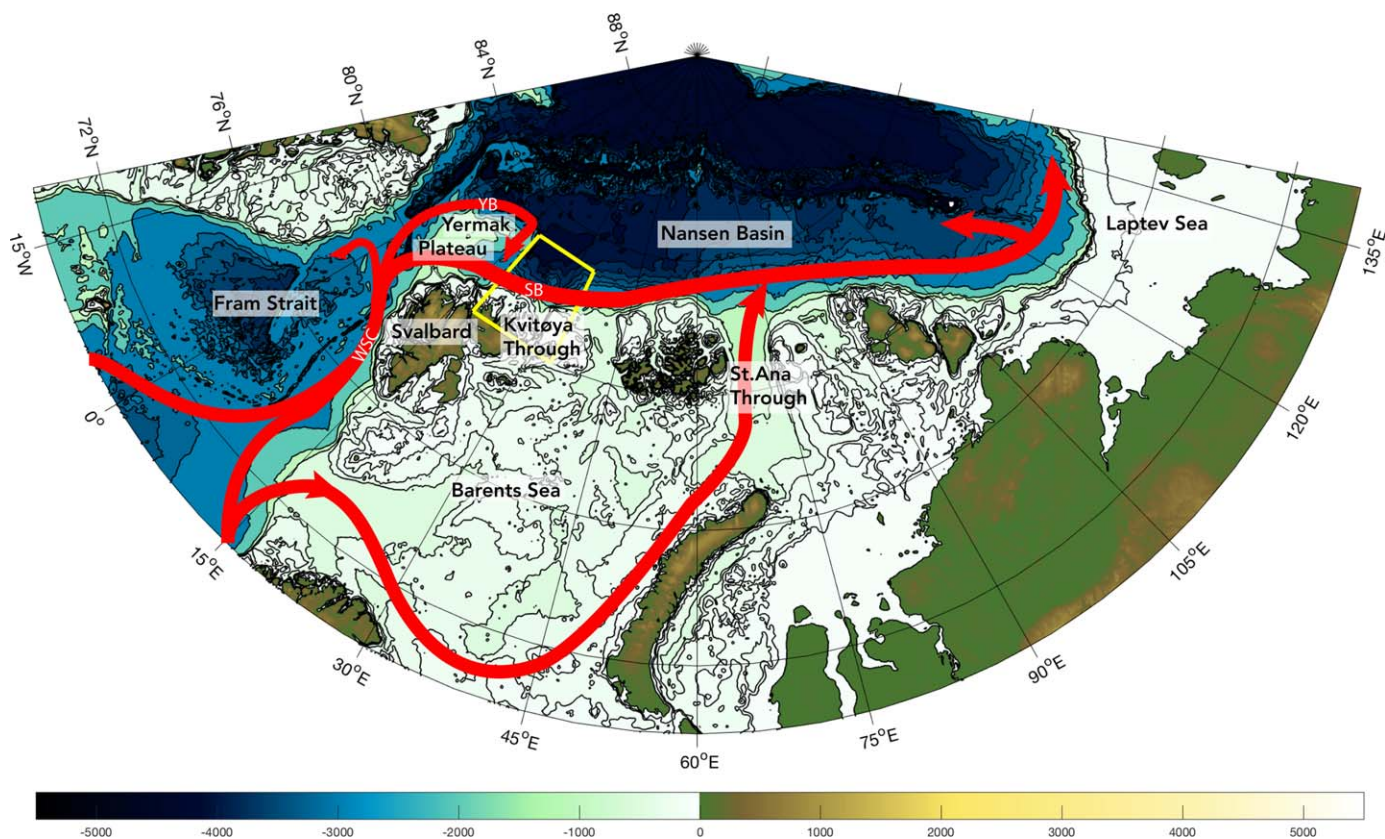

Figure 1. Geographical map of the region where Atlantic Water enters the Arctic Ocean. The schematic circulation of the Atlantic Water is indicated by the red lines. The West Spitsbergen Current (WSC) splits into a recirculation and two main branches: one flows around the Yermak Plateau (YB) and the other north of Svalbard (SB). The yellow box indicates the A-TWAIN study area shown in Figure 2. The IBCAO version 3 bathymetry is shaded according to the color bar.

winter over the upper slope at 30°E, while farther to the east *Dmitrenko et al.* [2006] and *Ivanov et al.* [2009] noted an annual warming/cooling of the AW on the continental slope during winter/summer, which is out of phase from the inflowing AW through Fram Strait [*Schauer et al.*, 2004]. *Dmitrenko et al.* [2006], focusing on the Laptev Sea continental slope, attributed this signal to lateral shifts of the AW core resulting from seasonal changes in the wind pattern. *Ivanov et al.* [2009], on the other hand, explained the seasonal cycle observed at 31°E by changes in the intensity of the upward heat flux from AW.

Moorings along the boundary current have also provided information about the propagation of signals emanating from Fram Strait. For example, *Polyakov et al.* [2011] suggested that an AW anomaly took roughly 5 years to propagate from Fram Strait to the Laptev Sea. The AW core decreases in temperature and salinity progressing through the Nansen Basin, becoming a layer of maximum 2°C and salinity of 34.9 [*Schauer et al.*, 2002; *Dmitrenko et al.*, 2015; *Rudels et al.*, 2015]. In addition, *Pnyushkov et al.* [2015] noted a reduction in the boundary current speed from 24 to 4 cm s^{-1} between Fram Strait and the Lomonosov Ridge. Notably, several studies have suggested that the circulation of AW emanating from Fram Strait is restricted to the Nansen Basin and that the remaining AW in the Arctic Ocean originates from the Barents Sea through St. Anna Trough [*Schauer et al.*, 2002; *Rudels et al.*, 2013, 2015]. In contrast to this, other investigations show evidence of AW from Fram Strait as far downstream as the Canadian Basin [*Woodgate et al.*, 2007; *Karcher et al.*, 2012].

The studies to date addressing AW north of Svalbard have focused mainly on temperature and salinity variability [*Aagaard et al.*, 1987; *Saloranta and Haugan*, 2001; *Cokelet et al.*, 2008]. It is known that this is an area with large ocean-atmosphere heat flux [*Cokelet et al.*, 2008], but also characterized by direct interactions between the warm AW and sea ice [*Polyakov et al.*, 2011; *Ivanov et al.*, 2012; *Rudels*, 2013; *Onarheim et al.*, 2014; *Rudels et al.*, 2015]. The AW is believed to influence the climate and ice conditions of Svalbard [*Walczowski and Piechura*, 2011]. *Våge et al.* [2016] recently investigated the kinematics of the AW boundary current in this region using a set of synoptic shipboard sections. In addition to their transport estimate, *Våge et al.* [2016] presented evidence of a small anticylonic eddy containing AW situated offshore of the current, arguing that the eddy was spawned by the current. This suggests that the boundary current is baroclinically unstable, consistent with the results of *Schauer et al.* [1997] and *Teigen et al.* [2011] using data from other regions. *Våge et al.* [2016] also discussed wind forcing of the current, but their data set was limited to two synoptic sections occupied across the current.

Our study focuses on the AW boundary current north of Svalbard using a shipboard hydrographic/velocity data set comprised of eight high-resolution transects across the current (Figure 2). This offers the best view to date regarding the structure of the current and how it varies progressing downstream. We also address the interaction of the current with the Kvitøya Trough, which cuts into the shelf in our study area. The paper begins with a description of the data set and the methods used in the analysis, particularly the technique for interpolating all of the sections onto the same grid, which allows us to compute a mean section. We then discuss the atmospheric conditions and sea ice distribution at the time of the field program and put this into context with the climatological conditions in this region. The water masses of the current are described next, followed by a presentation of the mean structure of the current, its alongstream variation, and its vorticity structure. Finally, the circulation in the Kvitøya Trough is investigated.

2. Data and Methods

2.1. Data

A total of 167 conductivity-temperature-depth (CTD) stations within the geographical area 80°N–83°N and 18°E–34°E were carried out from 15–28 September 2013 onboard the R/V *Lance* (Figure 2). The hydrographic cruise was part of the international project entitled "Long-term variability and trends in the Atlantic Water inflow region" (A-TWAIN) to investigate the AW north of Svalbard and its connection to Fram Strait. The project included a year-long mooring array centered at 30.5°E (along section B7 in Figure 2), and two hydrographic cruises—one during which the array was deployed (in September 2012 [see *Våge et al.*, 2016]) and the other during which the array was recovered. The shipboard data used in this study were collected on the second cruise (hereafter referred to as the A-TWAIN recovery cruise).

The hydrographic survey carried out during the A-TWAIN recovery cruise consisted of eight meridional sections extending from the outer shelf across the slope in order to sample the boundary current, and four
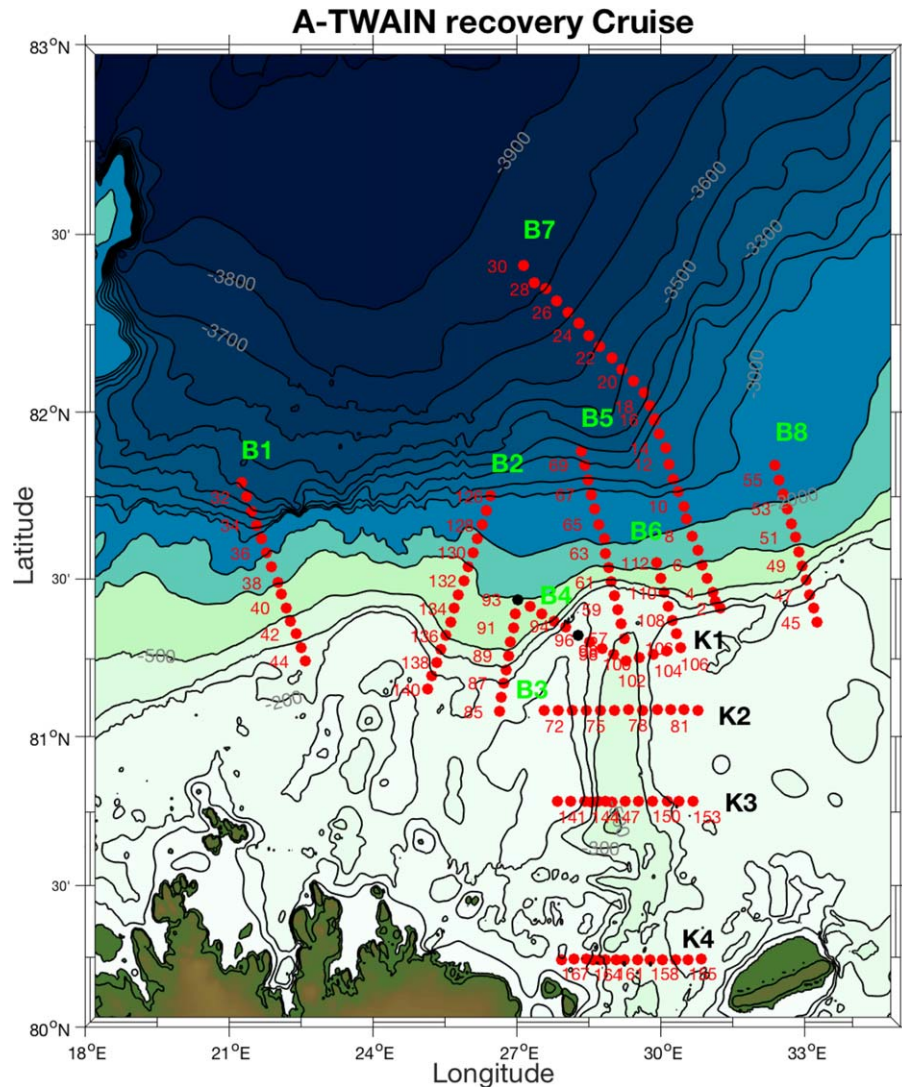
Figure 2. Shipboard hydrographic and velocity transects, where red dots denote station locations. Black dots correspond to those stations used in more than one transect. Black and green numbers enumerate the transects, while stations numbers appear in red. The bathymetry is the same as in Figure 1.

zonal sections across the Kvitøya Trough to assess the exchange with the Barents Sea (Figure 2). In most cases the casts extended from the surface down to 800 m, except for a subset of deep stations occupied for calibration purposes. A Sea-Bird 911+ CTD was used. The temperature sensor underwent a laboratory calibration before and after the cruise. To calibrate the conductivity sensor, we compared the data to the Sea-Bird SBE37 MicroCats of the moorings and to the 2012 calibrated CTD data. Deeper than 1200 m the temperature-salinity (T/S) relationship is very tight which allowed us to compute a conductivity slope correction to the 2013 data to bring it in line with the other two data sources. The resulting accuracies are deemed to be 0.001°C, 0.002 and 0.3 db for temperature, salinity, and pressure, respectively.

The ship was outfitted with a 150 kHz vessel mounted Broadband Acoustic Doppler Current Profiler (VMADCP) that provided measurements of velocity to roughly 200 m depth. The instrument was set up to collect 5 min averages of single ping data, one ping/second, using 8 m bins in narrowband mode. This set-up results in an instrument error of 0.41 cm/s for each 5 min ensemble. Although processed data were corrected for transducer misalignment errors using bottom track calibration, these calibration procedures serve to minimize transducer misalignment errors, not eliminate them. Therefore, in order to minimize errors due to transducer misalignment, which are dependent on ship speed, only on-station averages of VMADCP were used in our analysis. Errors from navigation and transducer misalignment contribute

approximately 0.5 cm/s to the instrument error. We thus estimate the total instrument error to be approximately 1.0 cm/s.

After processing, the barotropic tidal signal was subsequently removed from each on-station average using a 1/60th of a degree regional (75°N–85°N and 25°E–50°E) implementation of the OSU global barotropic tidal model TPXO (described in detail by *Egbert et al.* [1994] and further by *Egbert and Erofeeva* [2002]). There are two ways to use the tidal model to remove the tidal signal from our data: either by downloading the tidal components and filtering out each tidal harmonic signal from the data, or by using the direct output of the tidal model prediction program which calculates tidal velocities by dividing tidal transport by tidal model depth at each station. We chose to use the second approach as it already estimates the total contribution of all tidal components for each specific time and location. The largest uncertainty of the detided product is due to inaccurate bathymetry in the tidal model. We compared the bathymetry of the model to the measured depths at each station and estimated the corresponding velocity error to be 1.8 cm/s. Hence, the total bias error in velocity (instrument error plus tidal model error) is taken to be 2.8 cm/s. The other source of error in velocity, the random error due to unresolved scales [*Gomis and Pedder*, 2005], was estimated by using a bootstrap method [e.g., *Efron and Tibshirani*, 1994]. The total uncertainty in transports presented below is then computed as the error propagation sum of the bias and random errors.

To assess the atmospheric conditions during the cruise, the ERA-Interim daily global atmospheric reanalysis fields were used. This product has a spatial resolution of 0.75° and temporal resolution of 12 h [*Dee et al.*, 2011]. The data were obtained from the European Centre for Medium Range Weather Forecast public data sets (http://apps.ecmwf.int/datasets/). The bathymetry used in the maps is from the International Bathymetric Chart of the Arctic Ocean version 3 (IBCAO) [*Jakobsson et al.*, 2012], while the bathymetric data used in vertical sections were obtained from *Lance's* EK60 echo sounder.

The Arctic-wide Sea Ice concentration is obtained from the Sea Ice Trends and Climatologies from SMMR and SSM/I-SSMIS version 1 [*Cavalieri et al.*, 2004; http://nsidc.org]. This data product from passive microwave instruments is available in a stereographic projection at a grid cell of 25×25 km. For the local ice coverage, MASAM2 [*Fetterer et al.*, 2015] is used which is a 4 km resolution sea ice concentration product that blends ice extent from the Multisensor Analyzed Sea Ice Extent (MASIE) product and ice concentration from the Advanced Microwave Scanning Radiometer 2 (AMSR2). The sea ice data were downloaded from the National Snow and Ice Data Center (https://nsidc.org/data/docs/noaa/g10005-masam2/).

2.2. Methods

Vertical sections of potential temperature, salinity, and potential density were created using Laplacian-spline interpolation with a grid spacing of 2 km in cross-stream distance (x) and 2 m in depth (z). Since the bottom topography varies from transect to transect, in order to construct average meridional vertical sections each gridded transect was then transformed into a bottom depth versus height above 800 m coordinate frame following *Pickart* [1992] (recall that 800 m is the deepest common depth of all of the sections). After the transformation, the sections were interpolated again in the new coordinate frame with a grid spacing of 50 m in bottom depth and 25 m in height above 800 m. In all cases the main hydrographic features of the section were accurately captured in the new coordinate system. Finally, an average cross-slope bottom profile was computed using the eight transects following the procedure in *Pickart* [1992]. This way, the mean sections can be plotted in the familiar distance versus depth coordinate frame by applying the reverse transformation using the average bottom.

Absolute geostrophic velocities were calculated by referencing the thermal wind shear using the VMADCP data, following the method of *Comas-Rodríguez et al.* [2010]. For each station pair, the average VMADCP profile was computed. Then the geostrophic profile was matched to the VMADCP profile over the depth range where the shear was similar for the two profiles. This served to exclude near-surface regions where ageostrophic signals might be significant. Vertical sections of absolute geostrophic velocities were created following the same procedure as that for the hydrographic variables.

3. Atmospheric and Sea Ice Setting

It is of interest to characterize the atmospheric forcing and presence of sea ice during the A-TWAIN recovery cruise to see if the conditions were anomalous in any way.

3.1. Wind and Sea Level Pressure

The climatological mean sea level pressure (SLP) distribution during the second half of September (from 1979–2015) is dominated by a trough that extends from the vicinity of Iceland to the northeast into the Barents Sea (Figure 3a). This is indicative of the North Atlantic storm track [*Bengtsson et al.*, 2006]. The winds along the storm track are variable (i.e., low-directional constancy [e.g., *Pickart et al.*, 2013]), which means that there is no preferred wind direction; hence, the mean tends to be small. This is consistent with the band of low mean wind speed along this path (Figure 3b). It also indicates that winds in the vicinity of our shipboard survey (and the mooring array) are normally relatively weak during this time of year.

During the A-TWAIN recovery cruise the situation was quite different in that the northeast part of the domain was dominated by high SLP (Figure 3c). The center of the high SLP migrated slowly to the southeast during the time period of the cruise and acted as a block to low-pressure systems that, based on the climatology, would otherwise have progressed to the northeast. We verified this by tracking the three storms that were present in the region during the time period of our cruise, using an automated routine with the
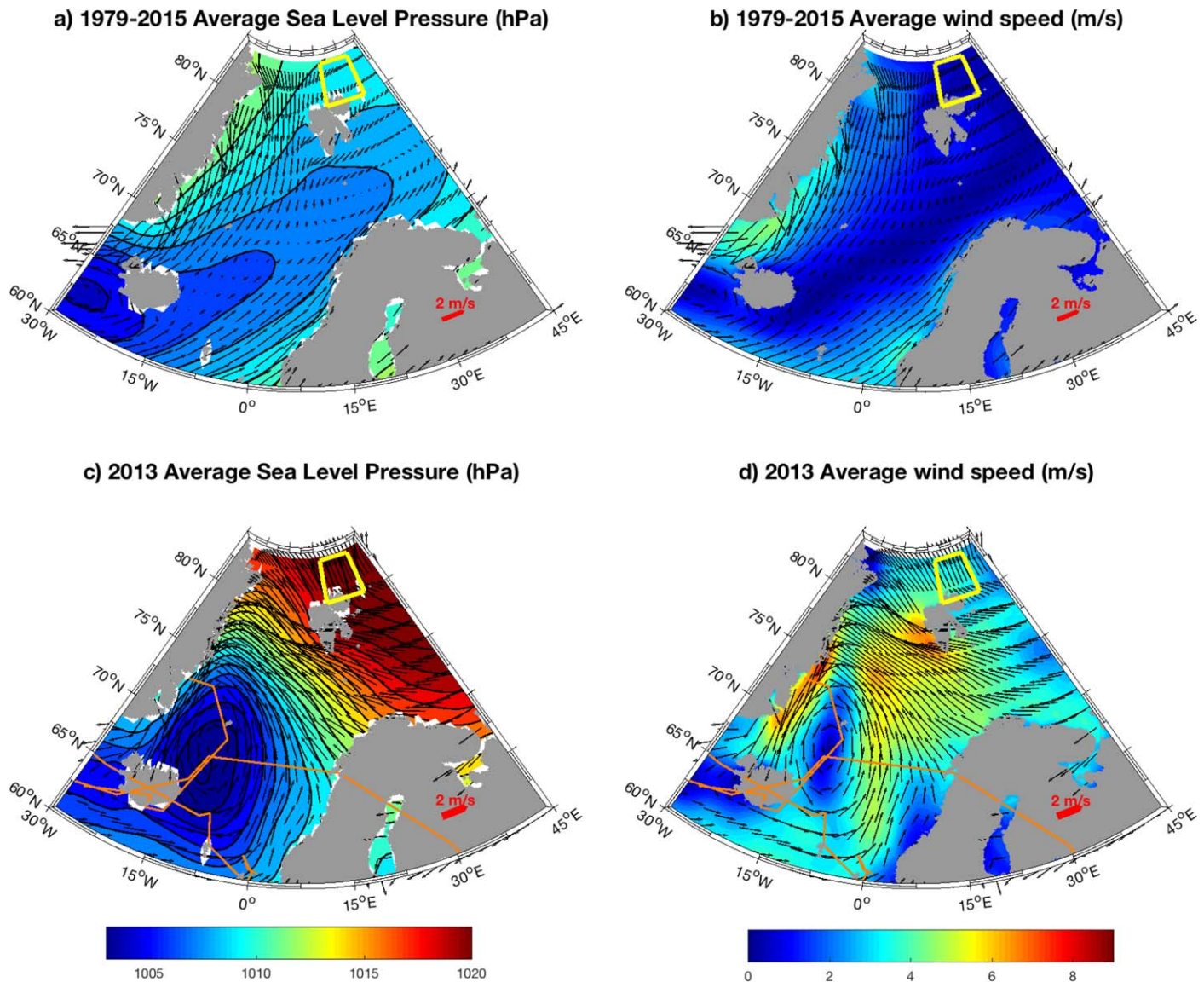

Figure 3. (top row) Climatological average sea level pressure (left, color) and 10 m wind speed (right, color) from ERA Interim for the time period 15–28 September (period of the A-TWAIN recovery cruise). The 10 m wind vectors are included. The yellow box represents the study area. (bottom row) Same as top row except for 2013 (when the cruise took place). The orange lines indicate the tracks of the three storms that occurred during the time period of the cruise.
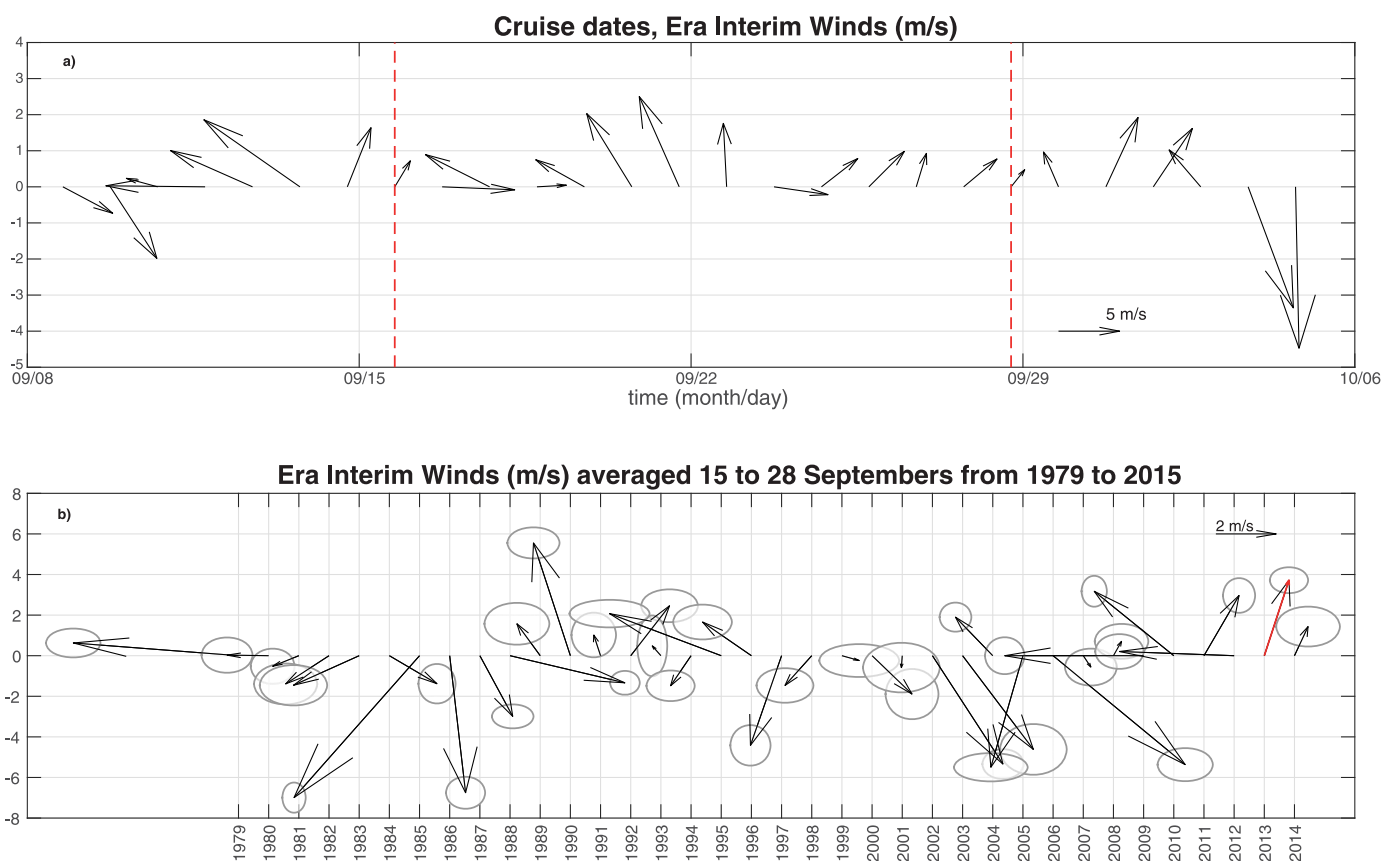
Figure 4. ERA Interim winds at 28.50°N, 81.75°W near the center of our study domain (middle of section B4, see Figure 1). (a) Time series of 10 m winds from 1 week before the cruise to one week after (the period of the cruise is indicated by the red dashed lines). (b) Average 10 m wind vector for 15–28 September (period of the cruise) for each year from 1979 to 2015 together with its standard error ellipse (the cruise year is highlighted as a red arrow).

ERA Interim data. In each case the storm veered toward the east or west without reaching the Svalbard area (Figures 3c and 3d). The gradient in SLP between the blocking high and these transient storms led to a region of strong winds southeast of Svalbard, but this did not affect the A-TWAIN study area (Figure 3d).

The daily time series of wind in the center of our study region reveals that the wind speed did not exceed 10 m/s during the cruise (Figures 4a and 4b). The generally southerly direction might have helped to keep the area ice free, moving it northward, although the average speed over the time period of the survey was only 3.8 m/s. As such, the Ekman transport was weak and did not significantly influence the volume transport at any of the sections (Table 1). To put this in context, we constructed a time series of wind averaged over the latter-half of September for each year using the ERA-Interim record (Figure 4c). The first thing to note is that at this time of year, there is no prevailing wind direction. Second, there was nothing extraordinary about the southerly winds in September 2013. The variable direction of the winds in this time series is consistent with the notion that our study domain is near the North Atlantic storm track and is generally influenced by passing low-pressure systems (Figures 3a and 3b). Interestingly, the northerly winds tend to be stronger than the southerly winds. This deserves further investigation (but is beyond the scope of our study).

Table 1. Estimated Ekman Transports for Each Transect

Transect	Ekman Transport (Sv)
B1	0.09 ± 0.03
B2	0.10 ± 0.03
B3	0.03 ± 0.01
B4	0.01 ± 0.01
B5	0.08 ± 0.03
B6	0.02 ± 0.01
B7	0.37 ± 0.10
B8	0.05 ± 0.02
K1	-0.00 ± 0.01
K2	-0.01 ± 0.01
K3	-0.01 ± 0.01
K4	-0.00 ± 0.01

3.2. Ice Coverage

Based on the SMMR, SSMI/I-SSMIS version 1 climatology from September 1988 to 2014, most of our study domain has some degree of ice cover during the month of September, ranging from 10% in the southwest corner to a 100% in the northern side of the study area (Figure 5a). In fact, there is typically only a narrow swath of open water immediately north of Svalbard, likely due to the advection of warm AW eastward from Fram Strait. By contrast, in September 2013 much of the Nansen Basin and Russian shelves were ice-free, including our study area (Figure 5b). Zooming into the region sampled by the ship (Figure 5c, MASAM2 ice product), one sees that there was no sea ice on the shelf or slope at any time during the survey. In fact, the ice edge receded roughly 160 km north of our measurement area (although the very northern stations of sections B1 and B7 could have experienced some ice cover (<5%) during the time of the survey). At this point most of the Yermak Plateau was ice-free as well, along with the eastern side of Fram Strait.

To assess the seasonality of ice cover in the region of our CTD survey during 2013, we used the MASAM2 ice product (Figure 6). September (the month of our survey) was the only month that year where the entire domain was ice-free. The ice cover was close to 100% during the months of March–June, but by August the concentrations had diminished considerably. Notably, during January the ice concentration diminished to
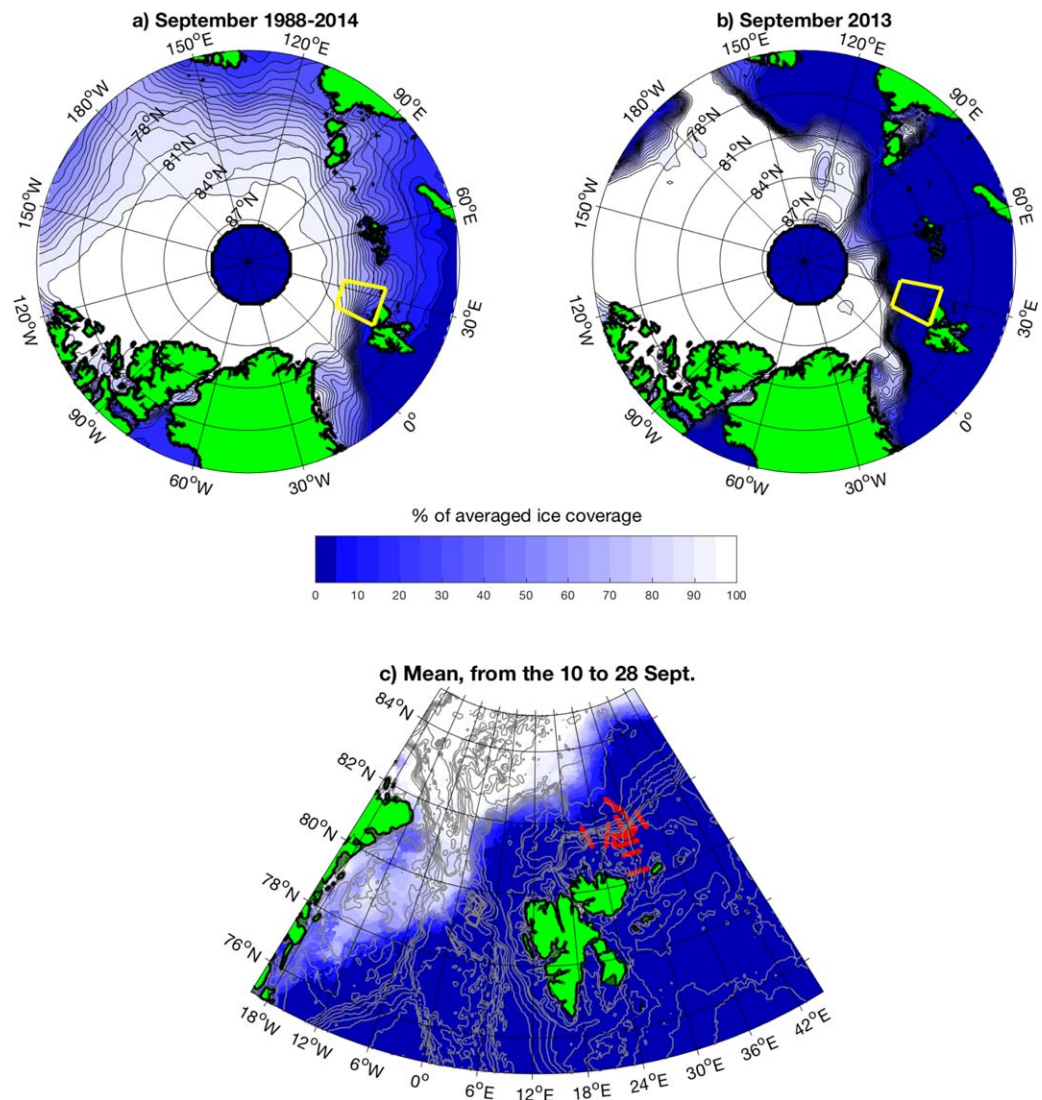

Figure 5. Ice concentration from SMMR, SSMI/I-SSMIS version 1 averaged for (a) September 1988–2014 and (b) September 2013. The yellow box indicates the A-TWAIN study area. (c) Enlarged view of the A-TWAIN study area showing the average ice concentration from MASAM2 during the time of the cruise. Red dots indicate the cruise stations and gray contours represent bathymetry.
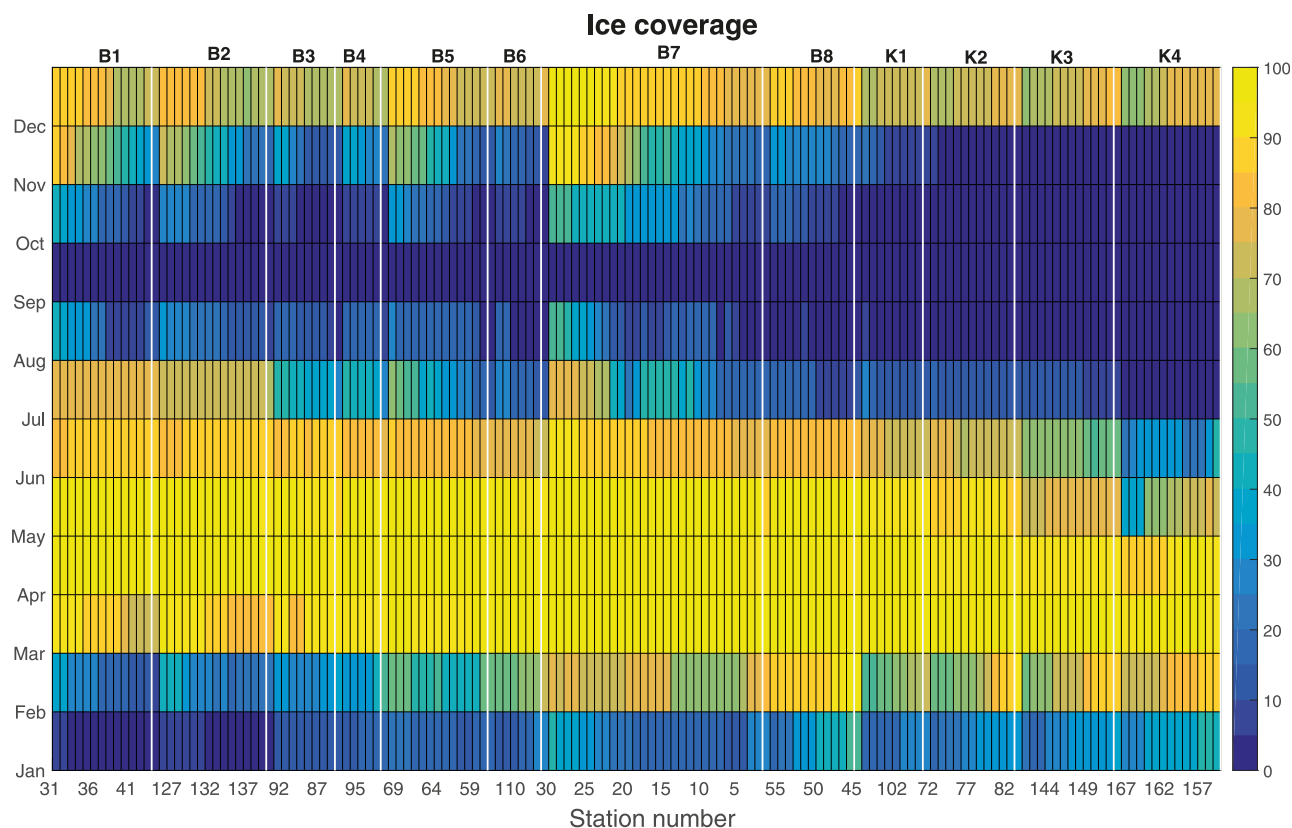
Figure 6. 2013 monthly percentage of ice coverage from MASAM2 at the location of the A-TWAIN-recovery cruise CTD stations. White lines indicate the limits in between the sections labeled above. The order of the stations is north to south for the meridional sections (B1–B8) and west to east on the zonal sections at the Kvitøya Trough (K1–K4).

<50%, and there was even open water in some parts of the study area. It is unlikely that this was due to the wind, which was weak during that month. On the other hand, the ice in the area north of Svalbard is generally first year and is under the impact of the AW [*Ivanov et al.*, 2012; *Onarheim et al.*, 2014]. The data from the A-TWAIN mooring array suggest that there was an increase in the advection of AW during the months of November and December which might have led to ice melt (A. Renner, personal communication, 2016).

4. The AW Boundary Current North of Svalbard

4.1. Water Masses

Past studies have employed a number of different water mass names and definitions to describe the hydrography of the Nansen Basin; hence, there is no generally agreed upon terminology or set of water mass boundaries. Starting with the AW, there have been broad definitions, such as that used by *Nansen* [1902] who identified AW as a water mass warmer than 0°C between the depths of 200–800 m. *Aagaard* [1989] was more restrictive, using 2°C as a lower temperature limit and also requiring that the water be saltier than 34.8. *Rudels et al.* [2005] used two bounding isopycnals (27.7 and 27.97 kg m^{-3}) to classify the AW, and also distinguished between two types of AW: that which stems directly from Fram Strait (called "Atlantic Water") and that which has recirculated in the Arctic Basin for some time and hence has become colder (called "Arctic Atlantic Water"). Other studies have used this isopycnal definition as well [e.g., *Beszczynska-Möller et al.*, 2012; *Våge et al.*, 2016]. Here we choose not to resolve the two types of AW, partly because there is ambiguity in distinguishing them. Also, we choose a minimum salinity limit of 34.9 for the AW (Figure 7a); this was used in *Aagaard et al.* [1987], and also is very close to the 34.88 limit used by *Cokelet et al.* [2008].

The different water masses identified in our data set north of Svalbard are shown in both the T/S plane and vertical plane in Figure 7 and outlined in Table 2. There are five water types, all of which have been previously identified and discussed in the literature. The warm and salty AW is present across each of the
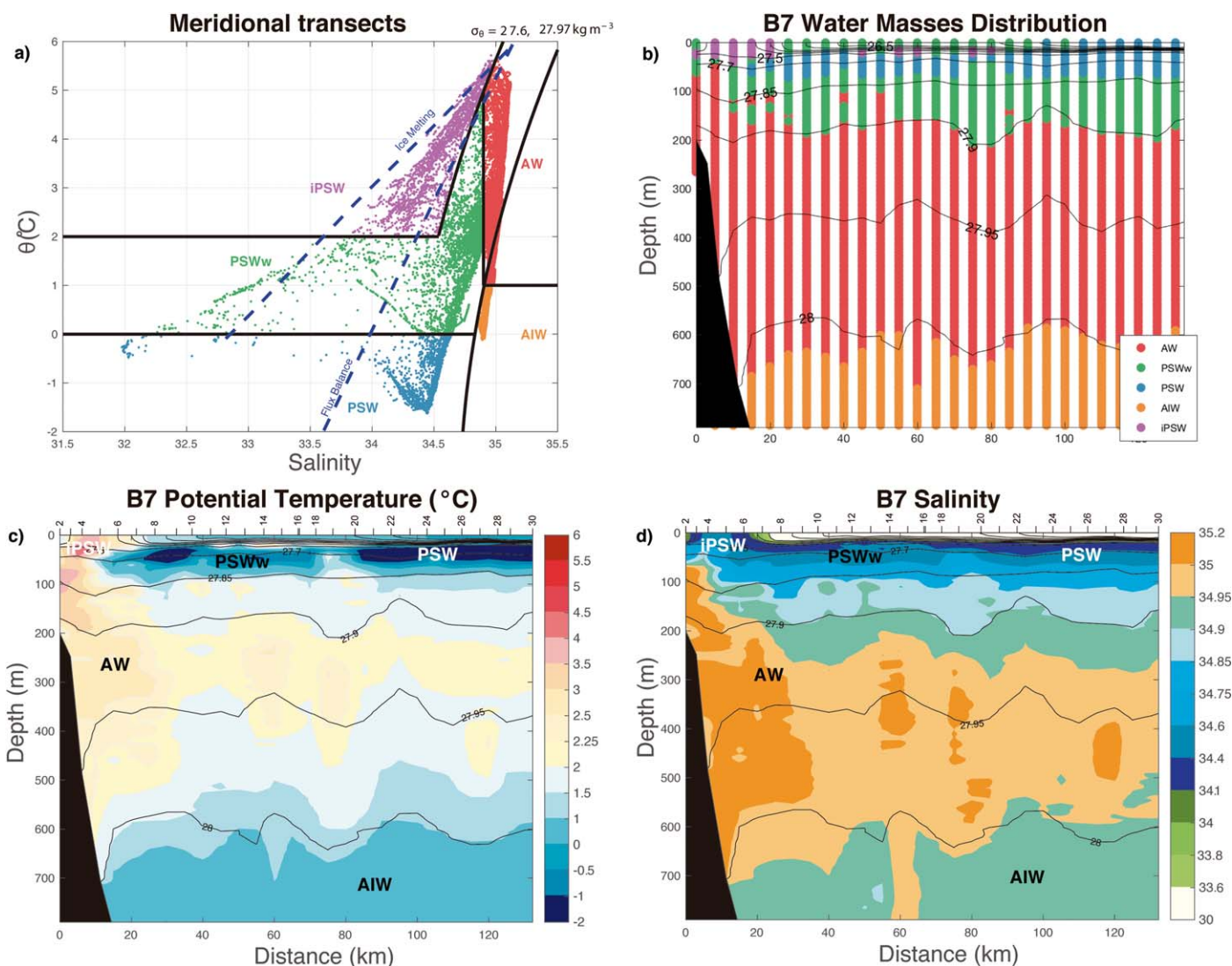
Figure 7. (a) Potential temperature/salinity diagram for all the meridional transects in the hydrographic survey (B1–B8). The different water masses considered in the analysis are distinguished by colors and labels. Various isolines of temperature, salinity, and density (27.6 and 27.97 kg m^{-3}) used in the definitions of the water masses are indicated (see text for details). Acronyms are in-shore Polar Surface Water (iPSW), warm Polar Surface Water (PSWw), Polar Surface Water (PSW), Atlantic Water (AW), and Arctic Intermediate Water (AIW). The blue dashed lines are ratios of atmospheric cooling against ice melt taken from *Cokelet et al.* [2008] for this area (discussed in the text). (b) Distribution of the different water masses in the vertical plane for section B7, based on the definitions in Figure 7a. (c) Vertical section of potential temperature (°C, color) overlain by potential density (kg m^{-3}, contours) for transect B7, including water mass names. (d) Same as Figure 7c except for salinity (color).

sections roughly between the depths of 150 and 700 m. In this geographical region the surface layer away from the continental shelf is comprised of Polar Surface Water (PSW) which originates in the Arctic Basin as mixture of AW, river runoff, precipitation, and ice melt [*Rudels*, 1989] (Figure 7). In general, our sections did not extend far enough into the basin to sample much of this water (the exception being section B7 which went beyond the 3800 m isobath). Over the midcontinental slope, a warmer variety of this mixture is called warm Polar Surface Water (PSWw), which is influenced to a greater extent by the warm AW [*Rudels et al.*, 2005].

During the A-TWAIN recovery cruise we sampled a particularly warm and Fresh water mass in the surface layer in the vicinity of the shelfbreak (purple color in Figures 7a and 7b). This water type has been noted previously [e.g., *Cokelet et al.*, 2008; *Tsubouchi et al.*, 2012; *Rudels et al.*, 2015] but does not have a name. Here we refer to it as inshore Polar Surface Water (iPSW). This is most likely a mixture of ice melt and AW, formed locally as well as upstream. In the T/S plane, most of this water falls in the region dominated by

Table 2. Water Masses Definitions

AW	$\sigma_\theta \geq 27.6$, $S \geq 34.9$, $\theta \geq 1$
iPSW	$27.6 \leq \sigma_\theta$, $\theta \geq 2$
PSWw	$\sigma_\theta \leq 27.97$, $0 \geq \theta \geq 2$, $S \leq 34.9$, and $\sigma_\theta \geq 27.6$, $S \leq 34.9$, $\theta \geq 2$
PSW	$27.97 \leq \sigma_\theta$, $\theta \leq 0$
AIW	$\sigma_\theta \geq 27.97$, $\theta \leq 1$

heat loss due to ice melt and in the vertical sections it always appears above the AW. *Cokelet et al*. [2008] considered the relative contributions to the modification of near-surface waters north of Svalbard due to atmospheric heat loss (sensible heat transfer) versus heat loss resulting from ice melt. Following *Cokelet et al*. [2008], we included two curves in Figure 7a (dashed blue lines) denoting how an AW end-member would evolve under the influence of ice melt alone (labeled as "ice melting") versus that due to equal contributions from ice melt and atmospheric heat loss (labeled as "flux balance"). As seen, the iPSW falls mostly between these two curves, implying a dominant contribution from ice melt. It appears that iPSW is the warmest fraction, or an early stage, of PSWw.

The final water mass in our data set is Arctic Intermediate Water (AIW). This is taken to be denser than 27.97 kg m^{-3} [*Aagaard*, 1989; *Rudels et al*., 2005] and cooler than 1°C (Figure 7a). The temperature limit is chosen because the AW enters the Arctic Ocean through Fram Strait over a wide depth range (from nearly 600 m depth to the surface) with temperatures higher than 2°C, and reaches the Lomonosov Ridge as an intermediate water mass with temperatures higher than 1°C [*Beszczynska-Möller et al*., 2012; *Dmitrenko et al*., 2008]. AIW is found immediately below the AW layer on all of our meridional sections.

4.2. Average Section

Using the procedure described in section 2.2, we computed the average sections of the hydrographic variables and absolute geostrophic velocity corresponding to the eight meridional transects (Figure 8). Most of the mean section is occupied by the warm and salty AW (delimited by the white dashed lines in the figure), which covers the approximate depth range of 75–700 m. The warmest part of the temperature core, however, is centered above this layer, associated with the iPSW, while the extremum in AW salinity is centered near 400 m depth. Farther offshore, seaward of about x = 40 km, there is cold and fresh PSWw in the upper 100 m (the mean section does not extend far enough northward to capture the colder PSW). The PSWw is the most strongly stratified water in the section (Figure 8c).

The mean absolute geostrophic velocity section (Figure 8d) provides the most robust view to date of the structure of the boundary current north of Svalbard—albeit over a time period of nearly 2 weeks. The current is roughly 40 km wide with a maximum eastward velocity of 20 cm/s. The flow decreases significantly with depth although it extends into the AIW layer (we have too little deep data to characterize the flow beneath 800 m). The configuration of the different water masses across the section is tied closely to the presence of the boundary current. In particular, the offshore edge of the current (near x = 40 km) corresponds to the edge of the warmest and saltiest AW as well as the transition from iPSW to PSWw in the layer above this. The geostrophic shear changes abruptly here as well; most notably, the isopycnals in the AW slope downward progressing onshore (corresponding to the decreased flow with depth). Similarly, at the onshore edge of the boundary current, near x = 12 km, the presence of AW decreases markedly, and, in the upper layer, there is a large presence of iPSW. The mean flow is quite weak here, and, in more than half of the sections, negative velocities are found in this region. (There is also westward flow at the offshore edge of the mean section, although only a few of the sections extended this far north.) Even though the region was ice-free during the time of our survey, it is important to note that, when averaged over the year, there is significant ice cover (increasing going offshore, Figure 8f). This may influence the structure of the boundary current; the mooring array data will shed light on this.

4.2.1. Volume Transport

Based on the mean velocity section shown in Figure 8, the total transport of the boundary current between the surface and 800 m is 3.11 ± 0.33 Sv. The AW portion of this is 2.31 ± 0.29 Sv. These estimated transports are a bit higher than the averages of the individual transects shown in Table 3 (although statistically they are comparable in light of the uncertainties). Based on two synoptic sections occupied in September 2012 along the A-TWAIN mooring line (section B7 in Figure 2), *Våge et al*. [2016] calculated an AW transport of only 1.6 ± 0.3 Sv. However, their definition of AW was more restrictive than that used here. Using a broader classification that is closer to ours, *Våge et al*.'s [2016] AW transport value increased to 1.8 ± 0.3 Sv, which is indistinguishable from our estimates taking into consideration the error bars. As seen in the vertical sections
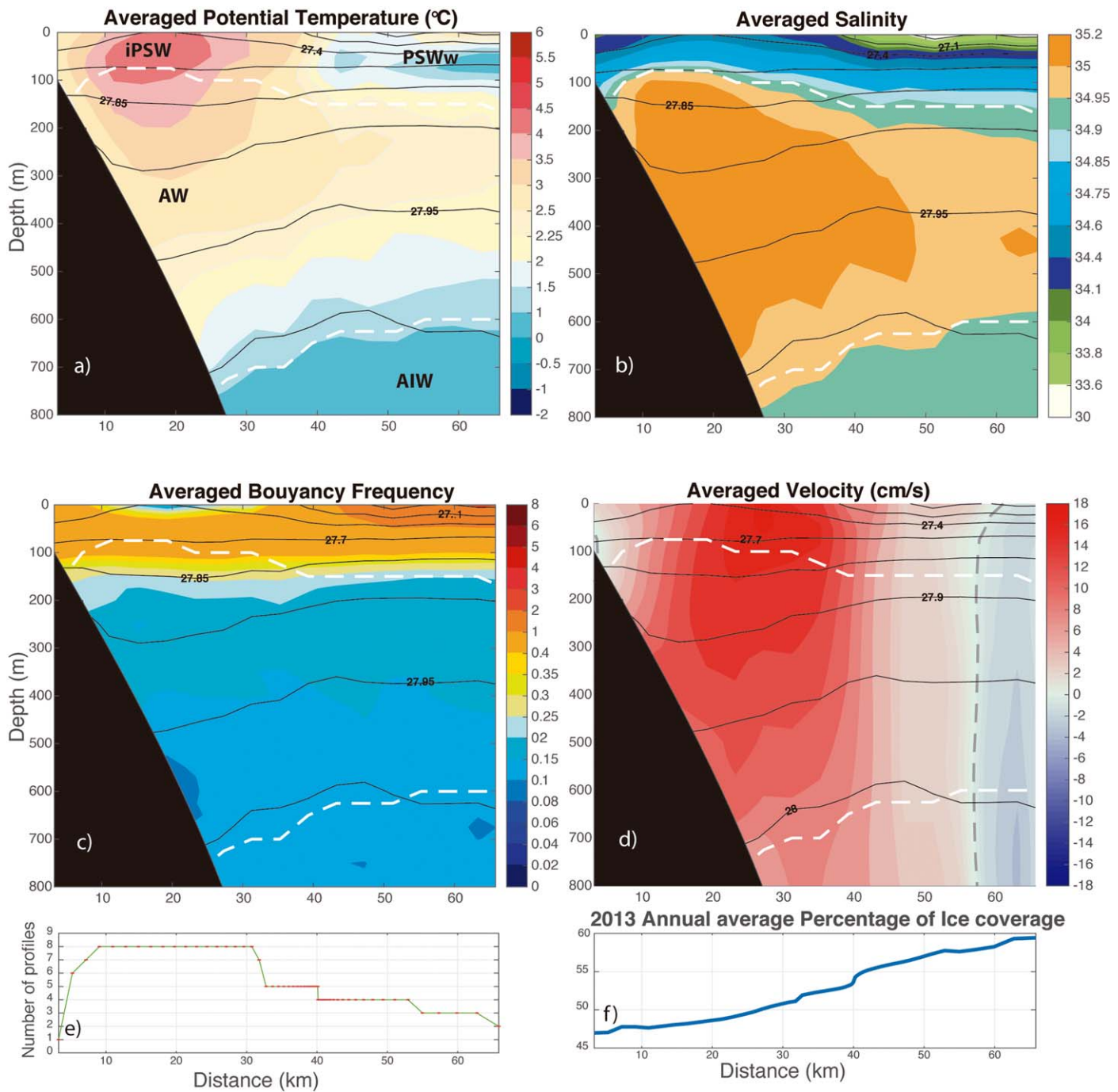
Figure 8. Mean vertical property sections constructed from the eight meridional transects. (a) potential temperature (color, °C) overlain by potential density (kg m^{-3}, contours); (b) salinity; (c) buoyancy frequency (s^{-2}); and (d) absolute geostrophic velocity (cm s^{-1}, positive is eastward). The dashed lines delimit the AW. Figures 8e and 8f show, respectively, the number of transects included in the average and the 2013 annual percentage of ice coverage, as a function of cross stream distance.

of Figure 8, the water that we have defined as AW is clearly part of the inflowing warm and salty water from the eastern side of Fram Strait. Because the T/S signature of the AW will become colder and fresher via mixing as it flows downstream, we believe that it is meaningful to compare our AW transport value to the obtained by *Beszczynska-Moller et al.* [2012] at 78.5°N in Fram Strait, estimated using a more restrictive T/S definition (water warmer than 2°C). The similarity of these two values, 3.0 ± 0.2 Sv at Fram Strait versus 2.31 ± 0.29 Sv north of Svalbard, implies that a significant portion of the Yermak branch of AW entering the strait has combined with the Svalbard branch by the time the two flows reach the longitude of 30°E.

Table 3. Estimated Mass Transports (Sv) Across the Different Meridional Sections for the Boundary Current (BC) and the Different Water Masses It Advects[a]

Transect	BC	AW	PSWw	PSW	iPSW	AIW
B1	3.42 ± 0.43	2.60 ± 0.34	0.36 ± 0.06	0.01 ± 0.01	0.21 ± 0.03	0.05 ± 0.01
B2	4.03 ± 0.28	3.39 ± 0.25	0.79 ± 0.05	0.01 ± 0.00	0.32 ± 0.02	0.18 ± 0.03
B3	0.90 ± 0.11	0.62 ± 0.08	0.42 ± 0.06		0.15 ± 0.02	0.00 ± 0.00
B4	2.26 ± 0.59	0.53 ± 0.16	0.23 ± 0.11		0.11 ± 0.05	0.00 ± 0.00
B5	3.10 ± 0.23	1.57 ± 0.12	0.70 ± 0.07	0.01 ± 0.00	0.18 ± 0.02	0.12 ± 0.02
B6	1.16 ± 0.54	1.58 ± 0.41	0.74 ± 0.23		0.34 ± 0.10	
B7	4.82 ± 0.26	2.58 ± 0.17	0.75 ± 0.05	0.09 ± 0.01	0.15 ± 0.02	0.38 ± 0.05
B8	1.96 ± 0.15	1.67 ± 0.13	0.38 ± 0.04		0.17 ± 0.02	0.00 ± 0.01
Average	2.71 ± 1.03	1.82 ± 0.66	0.55 ± 0.29	0.04 ± 0.01	0.20 ± 0.12	0.10 ± 0.06
Without (B3, 4, 6)	3.47 ± 0.62	2.36 ± 0.47	0.60 ± 0.12		0.21 ± 0.05	0.15 ± 0.06

[a]Also included are the average as well as the average without considering the short transects (B3, B4, and B6). Positive values indicate eastward transport.

The mean section of Figure 8 indicates that the boundary current north of Svalbard transports a significant amount of water above the AW layer. In particular, the transport of iPSW is 0.37 ± 0.10 Sv, and, offshore of this, the transport of PSWw is 0.36 ± 0.12 Sv. The iPSW can be thought as a younger stage of PSWw. It is well known that part of the AW evolves into a lighter surface layer north of Svalbard due to its contact with sea ice [*Rudels et al.*, 2004; *Cokelet et al.*, 2008; *Rudels et al.*, 2015]. This is the source of iPSW, but as this water mass flows eastward it mixes further with river runoff, precipitation, and ice melt. This mixing makes the water mass cooler and denser, ultimately becoming PSWw [*Rudels*, 1989].

The volume transport of the boundary current at each of the sections, including the contributions from the different water mass components, is listed in Table 3. Since two of the sections did not bracket the entire current, and in light of the high along-stream variability, we are unable to determine with any confidence if there is an along-stream trend in transport over the 180 km distance from sections B1–B8. There is, however, pronounced variability from section to section, which is discussed next.

4.3. Variability
Inspection of the individual vertical sections reveals that the boundary current north of Svalbard meanders as it flows eastward. To demonstrate this, we tabulated the lateral distance of the core of the current (where the maximum speed is determined within the AW layer) from the 300 m isobath (Figure 9a). One sees that the current can go from being centered near that isobath to being located roughly 30 km farther offshore. Notably, there is a systematic change in the structure of the current when it meanders. This is shown most clearly by contrasting two extreme realizations, section B2 (when the current is far onshore) and B1 (when the current is far offshore), which are displayed in Figure 10. When the current is close to the continental slope it is more barotropic, has increased stratification, and the central part of the AW layer is thinner. By contrast, as the current shifts offshore it becomes more surface intensified, more weakly stratified, and the AW layer expands within the current. In its offshore state the current develops a second, deeper velocity core adjacent to the continental slope, which is bottom intensified. This was the case in the four seaward-most realizations, and there is a signature of this in the mean section (near $x = 15$ km in Figure 8). Further work is required to understand the nature and cause of this deeper core.

The hydrographic characteristics of the center of the boundary current also display mesoscale variability. The temperature and salinity of the AW core vary from section to section, generally compensating each other in density (Figure 9b). While there is a slight trend of cooling/freshening progressing downstream, it is not statistically significant. There is also no apparent visual relationship between the meandering of the current and its core properties. The iPSW layer above the AW displays T/S variability from transect to transect, with its temperature fluctuations following that of the AW (Figure 9c).

4.4. Vorticity Structure of the Current
The fact that the AW boundary current meanders as it flows downstream motivates us to consider the potential vorticity structure of the current. *Spall et al.* [2008] demonstrated that the Pacific Water boundary current in the Beaufort Sea is baroclinically unstable and consequently forms eddies that ventilate the upper halocline of the Canada Basin. *Våge et al.* [2016] observed small eddies of AW offshore of the boundary
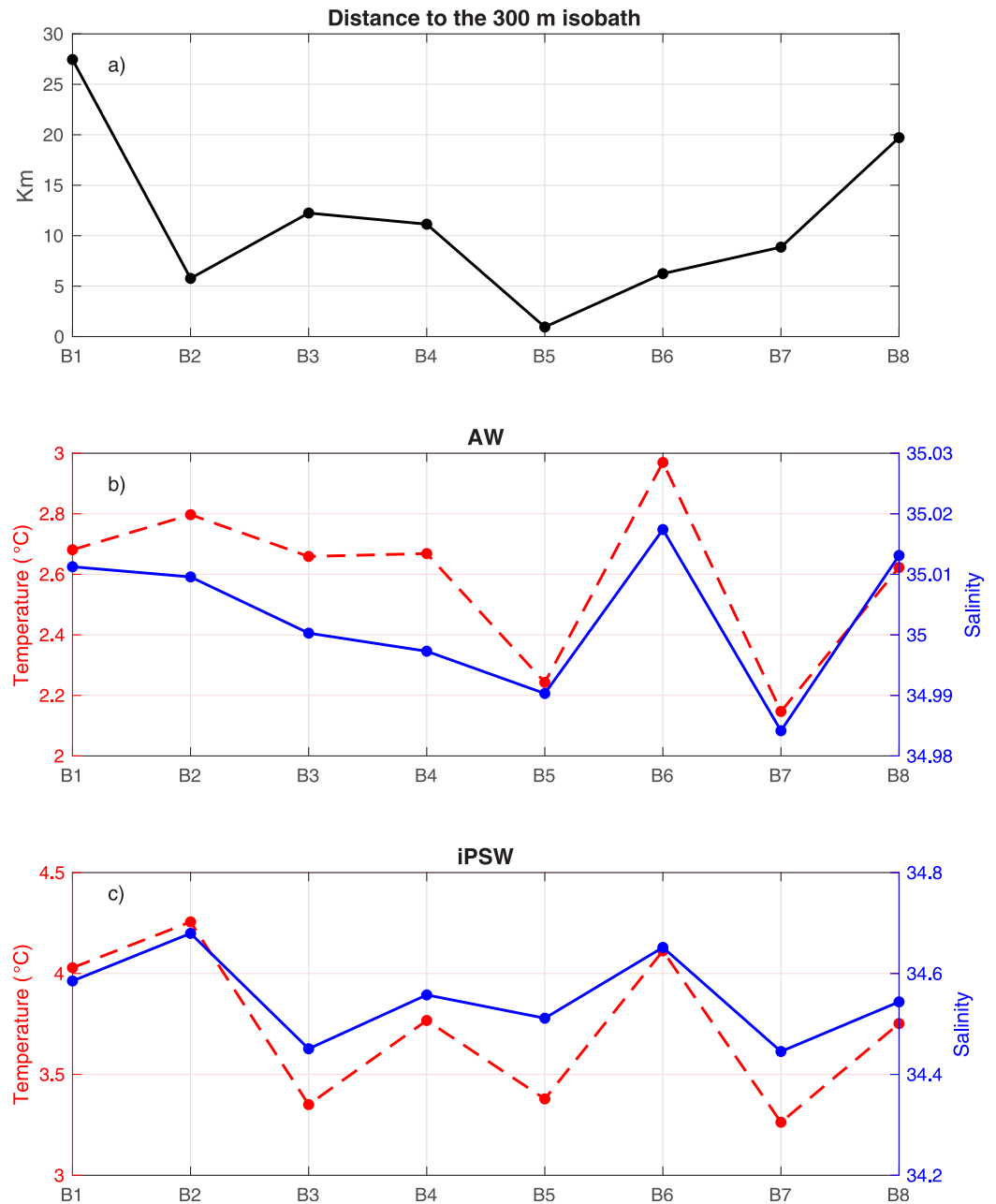
Figure 9. (a) Distance of the core of the boundary current from the 300 m isobath for each of the meridional transects. (b) Averaged temperature (dashed red line) and salinity (solid blue line) of the AW within the core of the boundary current at each transect. (c) Same as Figure 9b for iPSW.

current in the A-TWAIN study area and suggested that a similar process might be occurring there. In order to assess this, we computed the mean vertical section of Ertel potential vorticity using the mean hydrographic and velocity fields from Figure 9. The Ertel potential vorticity (Π) can be expressed as

$$\Pi = \frac{-f}{\rho_0}\frac{\partial \sigma_\theta}{\partial z} + \frac{1}{\rho_0}\frac{\partial u}{\partial y}\frac{\partial \sigma_\theta}{\partial z} - \frac{g}{\rho_0^2 f}\left(\frac{\partial \sigma_\theta}{\partial y}\right)^2,$$ (1)

where f is the Coriolis parameter (1.44×10^{-4} s^{-1}), g is the gravitational acceleration, ρ_o is the reference density (1028 kg m^{-3}), and u is the absolute geostrophic velocity. The three components of Π are the stretching vorticity, relative vorticity, and tilting vorticity corresponding to the three terms in equation (1), respectively [see *Hall*, 1994] for details].
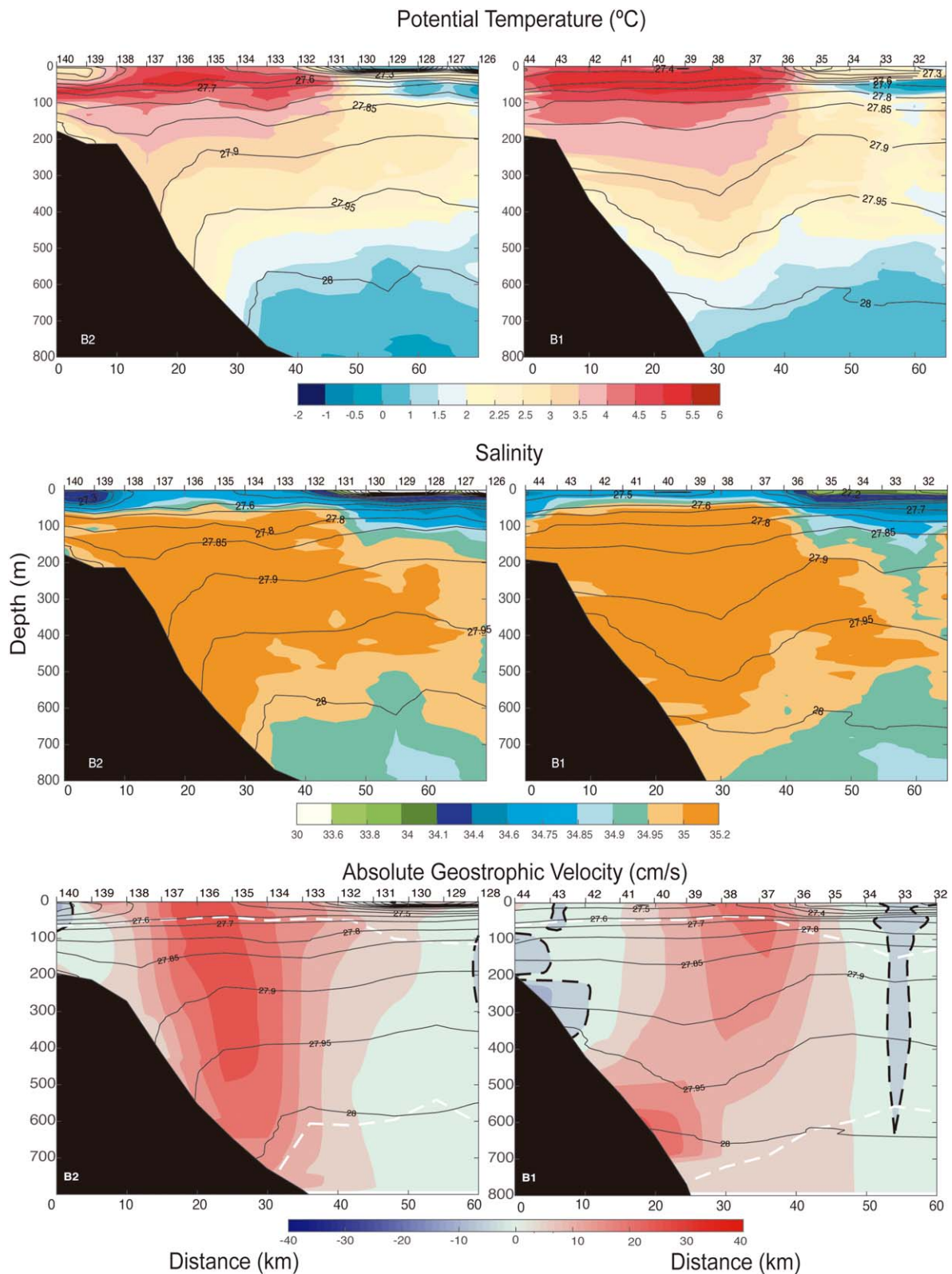
Figure 10. Vertical sections corresponding to the onshore (B2) and offshore (B1) extremes of the boundary current. (top) Potential temperature (color, °C) overlain by potential density (kg m^{-3}, contours); (middle) same except for salinity. (bottom) Same except for absolute geostrophic velocity (cm^{-1}, positive is eastward). The white-dashed lines delimit the AW, and the black dashed contours indicate the 0 cm^{-1} isoline.
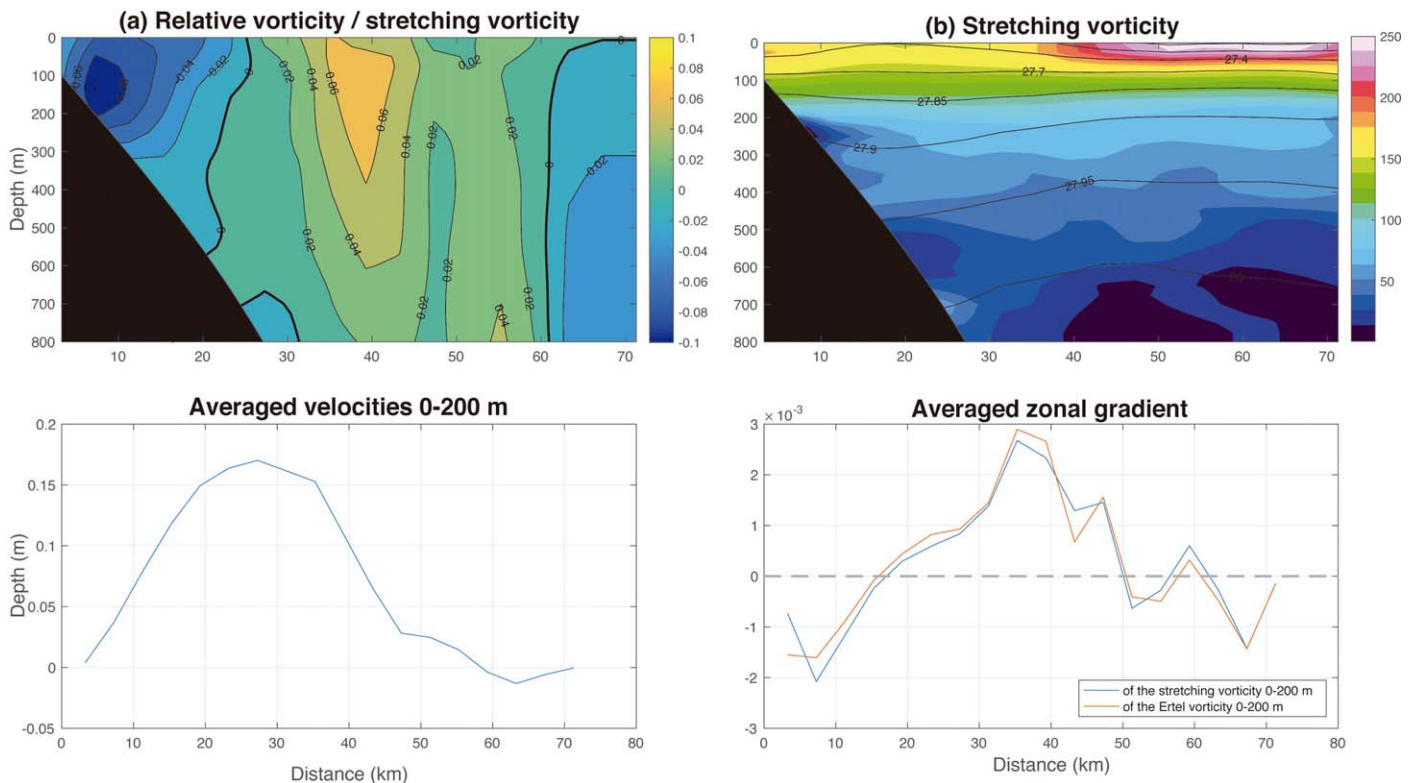
Figure 11. (a) Vertical section of the ratio of relative vorticity to stretching vorticity based on the mean sections of Figure 8. (b) Stretching vorticity (color, $(ms)^{-1}$) overlain by potential density (kg m^{-3}, contours). (c) Absolute geostrophic velocity averaged over the depth range 0–200 m. (d) Zonal gradient of the stretching vorticity and full Ertel potential vorticity averaged over the depth range 0–200 m (see legend).

The ratio of relative vorticity (normalized by f) to stretching vorticity of the mean section is shown in Figure 11 (the tilting term was negligibly small and is not shown). One sees that the anticyclonic vorticity on the inshore side of the current is slightly larger than the cyclonic vorticity on the offshore side, but both values are less than 10% of f. Hence, Π is dominated by the stretching term (as was the case also for the Pacific Water boundary current in the Beaufort Sea [see *Spall et al.*, 2008]). The cross-stream distribution of the stretching term reveals that the zonal gradient of Π changes sign within the current. In particular, in the upper 200 m, where the flow is strongest, $d\Pi/dy$ changes sign: on the anticyclonic side of the boundary current it is negative, while on the cyclonic side of the current it is positive (Figure 11d). In the deep part of the current this pattern in $d\Pi/dy$ is reversed. Hence, the AW boundary current north of Svalbard satisfies the necessary criterion for baroclinic instability.

As was true in the 2012 A-TWAIN hydrographic survey presented in *Våge et al.* [2016], we saw evidence in the 2013 A-TWAIN recovery cruise of eddy activity seaward of the boundary current. Only one of the sections extended into the basin (B7), and on this transect we sampled a cyclone (Figure 12). The feature was characterized by a slight bowling of the isopycnals in the upper 100 m and a more pronounced doming of the isopycnals below that. As such, the strongest flow is near 100 m with only weak velocities at a depth of 800 m. By contrast, *Våge et al.* [2016] observed several anticyclones with the opposite density structure—shallow doming and deep bowling of isopycnals—and a maximum azimuthal speed near 500 m. These anticyclones contained warm and salty AW in their cores, whereas the cyclone measured here corresponds to a pinching of the AW layer (Figure 12).

Our interpretation of the feature sampled in section B7 is that it is a near-field cyclone. When eddies are formed by a baroclinically unstable current they tend to emerge from the current in dipole pairs [*Spall*, 1995; *Bush et al.*, 1996]: the anticyclone contains boundary current water, while the center of the cyclone corresponds to ambient basin water (with boundary current water partially wrapped around it). Such dipole pairs then self-propagate, fluxing the boundary current water into the interior. Often the dipole pairs
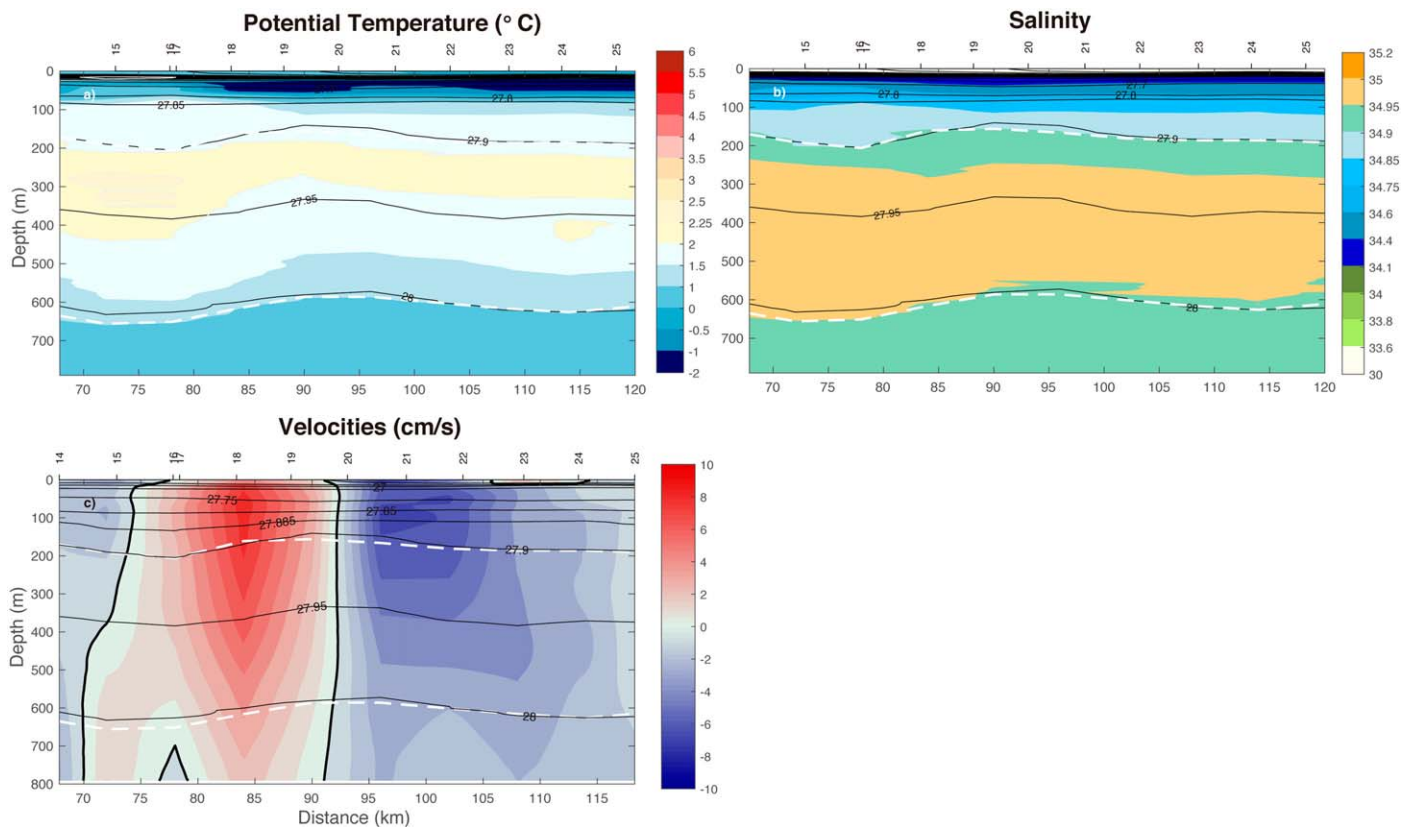
Figure 12. Vertical sections of properties for the outer portion of section B7 (see Figure 2 for the location of the section). (a) Potential temperature (color, °C) overlain by potential density (kg m^{-3}, contours). The white dashed delimits the AW. (b) Same as Figure 12a except for salinity. (c) Same as Figure 12a except for absolute geostrophic velocity. The thick black contours indicate the 0 cm s^{-1} isoline.

separate [e.g., *Spall et al.*, 2008], so it is not surprising to see either type of feature in isolation. Notably, the cyclone in Figure 12 is displaced vertically from the anticyclone of AW measured by *Våge et al.* [2016]. Its proximity to the surface suggests that the cyclone should spin down quickly due to friction from the pack-ice [*Ou and Gordon*, 1986] which covers the study area most of the year (Figure 6). This in turn implies that the deeper AW anticyclones should be longer-lived.

5. Kvitøya Trough

During the 2013 A-TWAIN recovery cruise we occupied a set of transects across the Kvitøya Trough to investigate whether part of the boundary current is diverted into the trough. Four zonal sections were occupied spanning a meridional distance of roughly 120 km (labeled K1–K4, Figure 2). From north to south the trough deepens from K1 (300 m) to K3 (450 m), then becomes abruptly shallower at K4 (250 m).

5.1. Water Masses

All of the water masses present in the boundary current sections along the continental slope were observed as well in the Kvitøya Trough (Figure 13a). This includes a small amount of AIW, even though this water mass was restricted to depths deeper than ∼600 m on the slope during the survey (the depth of the sill at the north end of the trough is approximately 250 m). AIW was present in K1, K2, and K3 but practically absent in K4. It was the only water mass denser than 27.97 kg m^{-3} in the deep part of the trough. This implies that, at times, upwelling from the slope can flux this dense water from the basin into the trough.

The vertical sections across the trough show the presence of AW on the western flank (Figures 13b and 13c). However, the AW is not nearly as abundant as along the continental slope (e.g., compare Figures 8 and 13). Furthermore, the signal of the AW erodes from north to south, and, by the southernmost transect K4, the signal is completely absent. The warm and fresh iPSW is also observed on the western side of the
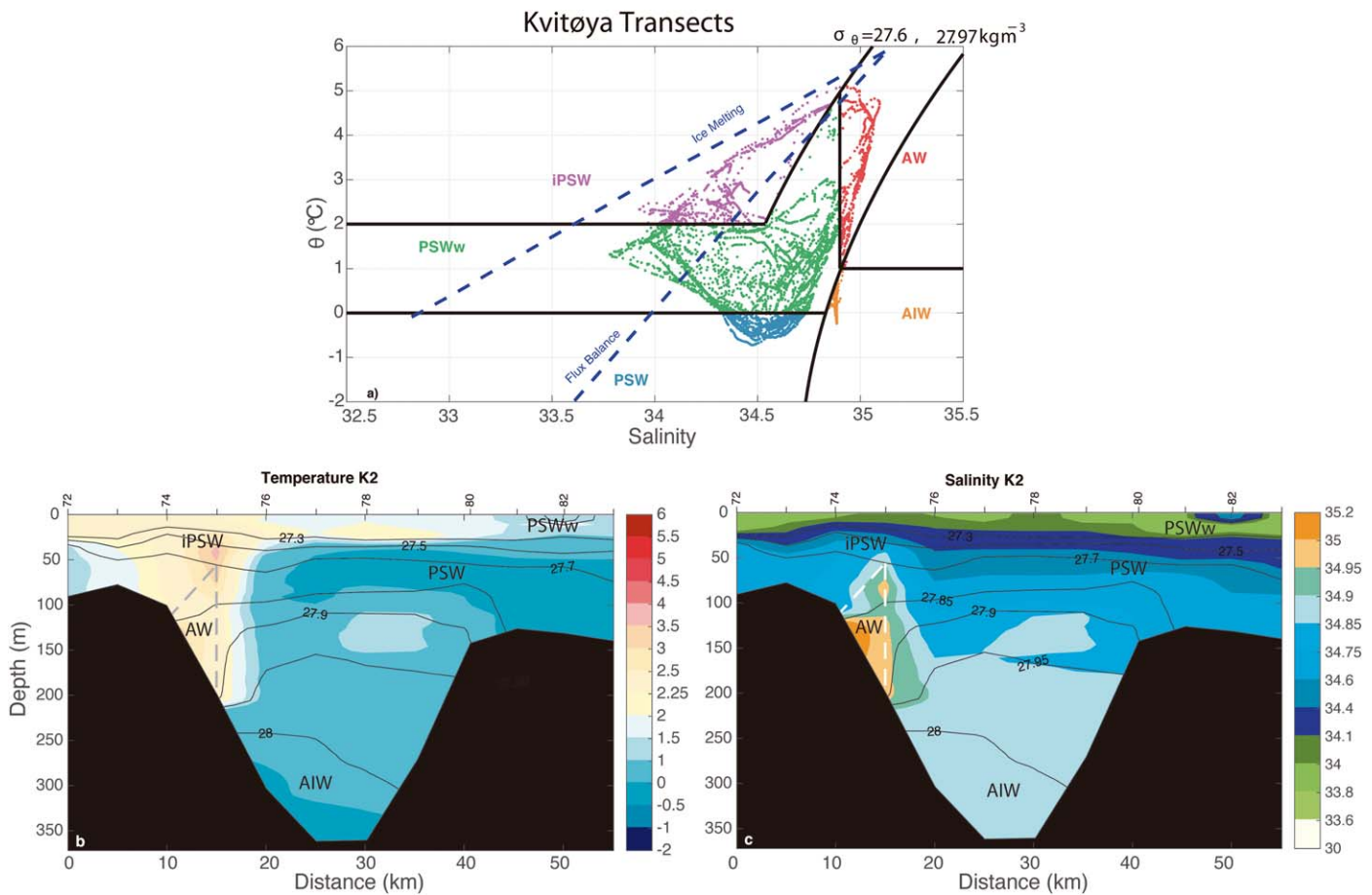
Figure 13. (a) Potential temperature/salinity diagram for of all the transects across the Kvitøya Trough. (b) Vertical section of potential temperature (color, °C) overlain by potential density (kg m^{-3}, contours) for section K2 across the Kvitøya Trough (see Figure 2 for the location of the section). The AW is delimited by the dashed line. (c) Same as Figure 13b except for salinity.

trough (Figure 13); in contrast to the AW, the signature of this water mass does not erode to the south. In fact, the largest portion of iPSW is found at K4. This implies that either the boundary current is not the only source of this melt/freshwater into Kvitøya Trough or that iPSW does not necessarily follow the same advective pattern as AW. Interestingly, both the AW and iPSW signatures are more confined to the boundary than for the sections across the continental slope. On the eastern flank of the trough a sizable tongue of PSWw is present between 50 and 100 m depth (Figure 13a, green).

5.2. Circulation

What do the velocity data tell us about the circulation within the trough? This is best illustrated by considering the VMADCP data. The depth integrated velocity vectors for the vicinity of the trough are shown in Figure 14a. Although we are unable to obtain an exact mass balance with our data, the vectors in the lateral map suggest a clear circulation pattern, which is outlined in the schematic of Figure 15. (We emphasize that the arrows in the figure are not streamlines; they are an interpretation of the general pattern of flow). It is evident that most of the boundary current progresses eastward along the continental slope past the trough, which is also indicated by the transport estimates along each of the meridional transects (Table 3). However, the velocity vectors imply that a portion of the current along its inshore edge turns and enters the trough. Some of this flow continues southward along the western side of the trough, but there also appears to be a recirculation or retroflection associated with the sharp bend in topography at the northwest edge of the trough (included in the schematic of Figure 15).

To the south of the moraine there is flow on both sides of the trough: southward flow along its western flank and northward flow along its eastern flank. Some of the southward flow exits the domain at section K4 (-0.26 ± 0.04 Sv), presumably part of a small throughflow from the Nansen Basin to the Barents Sea.
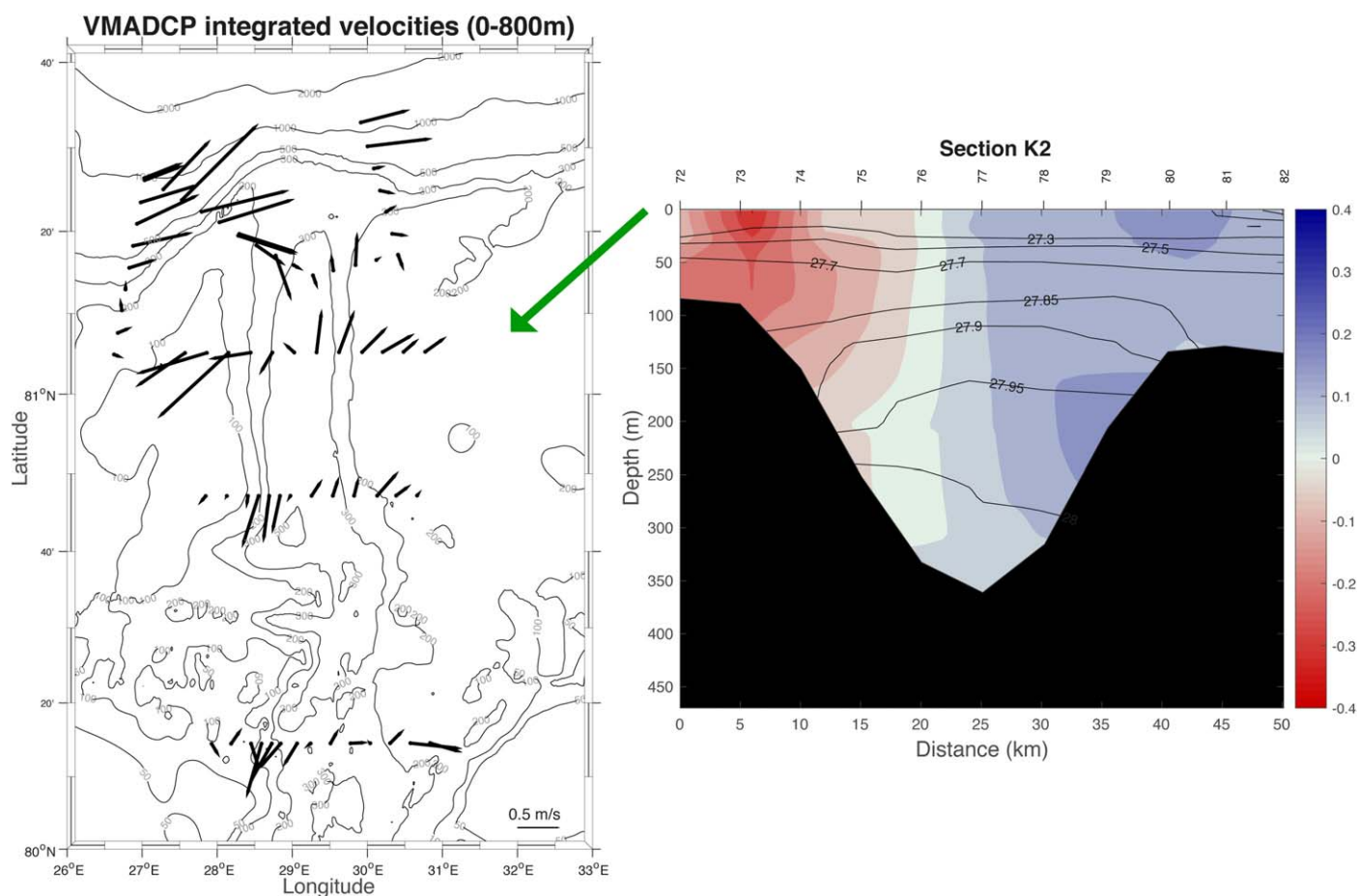
Figure 14. (left) Depth-integrated velocities from the vessel-mounted ADCP in the vicinity of the Kvitøya Trough. (right) Vertical section of absolute geostrophic velocity (cm s^{-1}, positive is southward) overlain by potential density (kg m^{-3}, contours) for section K2 across the Kvitøya Trough (see Figure 2 for the location of the section). Stations are shown along the top axis.

This is consistent with the 0.2 Sv reported by *Smedsrud et al.* [2010] east of our study area, in between Kvitøya Island and Franz Josef Land. The flow on the eastern side of the trough is partly due to a recirculation around the closed isobaths of the trough. This is evident in the vertical section of absolute geostrophic velocity at section K2 (Figure 14b) which shows compensating flows below sill depth (O(0.1 Sv) deeper than 250 m). It is also possible that some portion of the boundary current entering the trough recirculates around the deepest part to rejoin the boundary current (as indicated in the schematic). Overall, the T/S data from the zonal sections, together with the velocity data, suggest that only a small amount of AW enters Kvitøya Trough (approximately 0.2 Sv) and that this signal is quickly eroded via mixing. Hence, any boundary current water that is diverted into the trough—whether it enters the Barents Sea or recirculates back into the boundary current—is significantly transformed.

6. Summary

A hydrographic cruise carried out in September 2013, as part of the international A-TWAIN project, provided the most extensive view to date of the hydrographic and kinematic structure of the AW boundary current north of Svalbard. In addition, the cruise obtained the first high-resolution observations of the circulation in Kvitøya Trough. During the time period of the survey, a blocking high north of Fram Strait kept storms from propagating close to the study region, hence the winds were light and Ekman transports were negligible. There was no ice cover in the area.

Five water masses were identified in the data set, the dominant one being Atlantic Water (AW) which was present in the depth range of 75–700 m. Shallower than this was a mixture of AW, river runoff, precipitation, and ice melt of Arctic origin. This water mass is known in the literature as Polar Surface Water (PSW) and
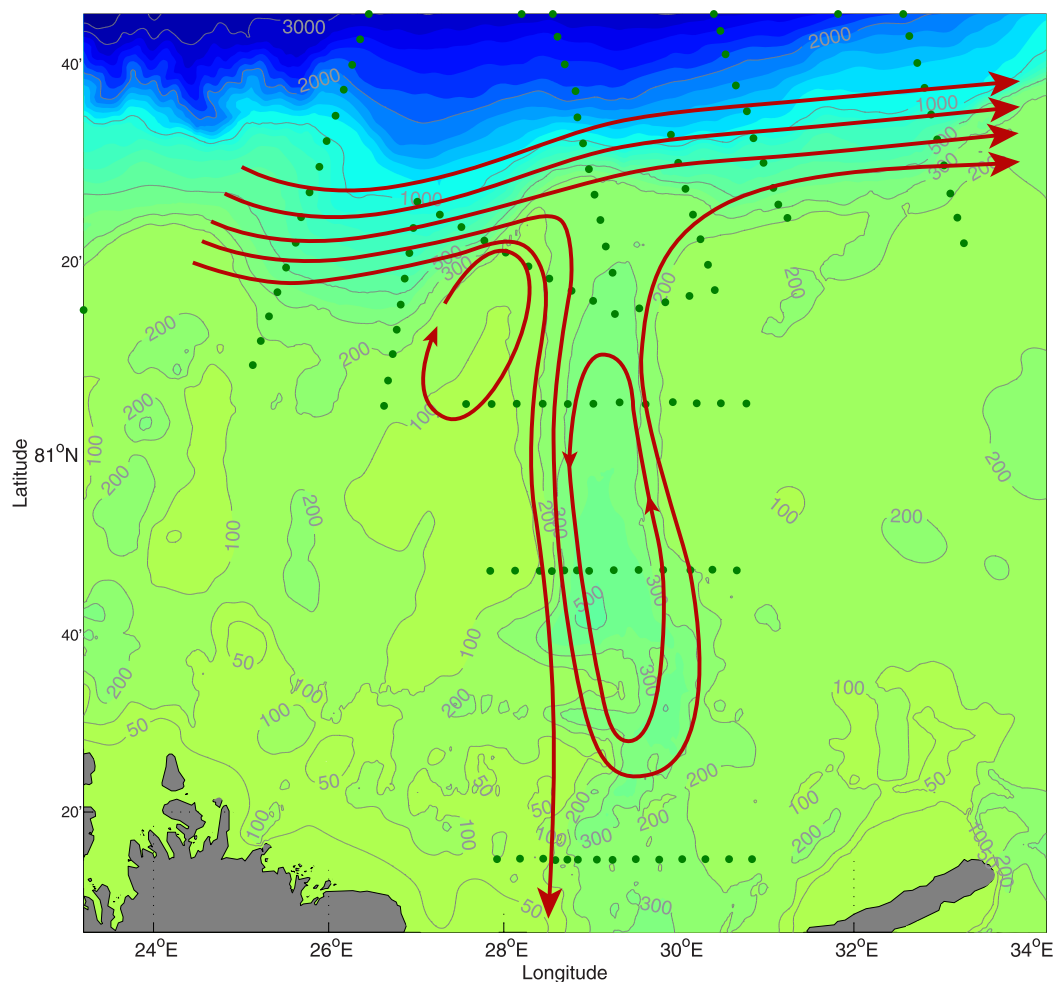
Figure 15. Schematic circulation of the Kvitøya Trough based on the depth-integrated velocity vectors in Figure 14a.

was present only in the offshore part of the domain. Over the continental slope a warm variety of PSW was found (PSWw), while farther inshore near the shelfbreak the PSW was influenced more strongly by ice melt (iPSW). Below the AW resided Arctic intermediate Water (AIW).

Using a bathymetric coordinate system, we interpolated each of the eight boundary current transects onto the same grid, enabling us to construct mean sections of hydrographic properties and absolute geostrophic velocity. This revealed that, on average, the boundary current is O(40 km) wide, surface-intensified, with an eastward transport of 3.11 ± 0.33 Sv. The mean flux of AW (2.31 ± 0.29 Sv) is comparable to the long-term mean value in Fram Strait reported by *Beszczynska-Möller et al.* [2012] (3.0 ± 0.2 Sv), suggesting that by 30°E the Svalbard Branch contains a significant contribution from the Yermak Branch. The boundary current also transports significant amounts of iPSW (0.37 ± 0.10 Sv) and PSWw (0.36 ± 0.12 Sv).

The individual transects in our survey suggest that the AW boundary current meanders as it flows eastward. During the offshore excursions the current becomes more baroclinic, more weakly stratified, and develops a second velocity core inshore and deeper than the main core. Such meandering is indicative of an unstable current, and it was shown that the meridional gradient of the mean Ertel potential vorticity changes sign across the current, satisfying the necessary condition for baroclinic instability. This in turn suggests that the current may spawn eddies in the form of dipole pairs [*Spall*, 1995; *Bush et al.*, 1996]. A previous study in this region observed middepth anticyclones of AW [*Våge et al.*, 2016], and our survey measured a surface-intensified near-field cyclone. It is reasonable to conclude that these eddy features emanate from the boundary current and represent an effective mechanism by which AW ventilates the interior Nansen Basin.

This is consistent with the results of previous studies farther to the east [*Schauer et al.*, 1997, 2002; *Woodgate et al.*, 2001].

Our survey suggests that a small portion of AW (approximately 0.2 Sv) enters the Kvitøya Trough and flows southward along its western flank. However, the water quickly loses its warm and salty signature and hence can no longer be termed AW. A portion flows through the southernmost transect of our survey, presumably entering the Barents Sea. There is also evidence of a closed recirculation around the deepest part of the trough. Overall, the presence of Kvitøya Trough does not seem to strongly impact the AW boundary current as it flows eastward along the continental slope, although one must keep in mind that our survey was just a single synoptic realization. More extensive measurements are needed to better quantify the interaction of the AW boundary current with this topographic feature.

References

Aagaard, K. (1989), *A Synthesis of the Arctic Ocean Circulation*, pp. 1–22, Le Conseil, Copenhague.

Aagaard, K., and E. C. Carmack (1994), *The Arctic Ocean and Climate: A Perspective*, 16 pp., AGU, Washington, D. C.

Aagaard, K., and P. Greisman (1975), Toward new mass and heat budgets for the Arctic Ocean, *J. Geophys. Res.*, *80*, 3821–3827.

Aagaard, K., A. Foldvik, and S. R. Hillman (1987), The West Spitsbergen Current: Disposition and water mass transformation, *J. Geophys. Res.*, *92*, 3778–3784.

Aksenov, Y., M. Karcher, and A. Proshutinsky (2016), Arctic pathways of Pacific Water: Arctic Ocean model intercomparison experiments, *J. Geophys. Res. Oceans*, *121*, 27–59, doi:10.1002/2015JC011299.

Bengtsson, L., K. I. Hodges, and E. Roeckner (2006), Storm tracks and climate change, *J. Clim.*, *19*, 3518–3543, doi:10.1175/JCLI3815.1.

Beszczynska-Möller, A., R. Woodgate, C. Lee, H. Melling, and M. Karcher (2011), A synthesis of exchanges through the main oceanic gateways to the Arctic Ocean, *Oceanography*, *24*, 82–99, doi:10.5670/oceanog.2011.59.

Beszczynska-Möller, A., E. Fahrbach, U. Schauer, and E. Hansen (2012), Variability in Atlantic water temperature and transport at the entrance to the Arctic Ocean, 1997-2010, *ICES J. Mar. Sci.*, *24*, 852–863.

Bush, A. B. G., J. C. McWilliams, and W. R. Peltier (1996), The formation of oceanic eddies in symmetric and asymmetric jets: Part II: Late time evolution and coherent vortex formation, *J. Phys. Oceanogr.*, *26*, 1825–1848, doi:10.1175/1520-0485.

Cavalieri, D., C. Parkinson, P. Gloersen, and H. J. Zwally (1996), updated yearly, in *Sea Ice Concentrations from Nimbus-7 SMMR and DMSP SSM/I-SSMIS Passive Microwave Data, Version 1*, [indicate subset used], NASA DAAC at the National Snow and Ice Data Center, Boulder, Colo. [Available at http://dx.doi.org/10.5067/8GQ8LZQVL0VL.]

Coachman, L. K., and C. A. Barnes (1963), The movement of Atlantic Water in the Arctic Ocean, *Arctic*, *16*, 8–16, doi:10.14430/arctic3517.

Cokelet, E. D., N. Tervalon, and J. G. Bellingham (2008), Hydrography of the West Spitsbergen Current, Svalbard Branch: Autumn 2001, *J. Geophys. Res.*, *113*, C01006, doi:10.1029/2007JC004150.

Comas-Rodríguez, I., A. Hernández-Guerra, and E. L. McDonagh (2010), Referencing geostrophic velocities using ADCP data at 24.5°N (North Atlantic), *Sci. Mar.*, *74*(2), 331–338.

Dee, D. P., et al. (2011), The ERA-Interim reanalysis: Configuration and performance of the data assimilation system, *Q. J. R. Meteorol. Soc.*, *137*, 553–597.

Dmitrenko, I. A., I. V. Polyakov, and S. A. Kirillov (2006), Seasonal variability of Atlantic water on the continental slope of the Laptev Sea during 2002–2004, *Earth Planet. Sci. Lett.*, *244*, 735–743, doi:10.1016/j.epsl.2006.01.067.

Dmitrenko, I. A., et al. (2008), Toward a warmer Arctic Ocean: Spreading of the early 21st century Atlantic Water warm anomaly along the Eurasian Basin margins, *J. Geophys. Res.*, *113*, C05023, doi:10.1029/2007JC004158.

Dmitrenko, I. A., et al. (2015), Atlantic water flow into the Arctic Ocean through the St. Anna Trough in the northern Kara Sea, *J. Geophys. Res. Oceans*, *120*, 5158–5178, doi:10.1002/2015JC010804.

Efron, B., and R. J. Tibshirani (1994), *An Introduction to the Bootstrap, Monogr. Stat. Appl. Prob.*, Chapman & Hall/CRC, Boca Raton, Fla. [Available at https://www.crcpress.com.]

Egbert, G. D., and S. Y. Erofeeva (2002), Efficient inverse modeling of barotropic ocean tides, *J. Atmos. Oceanic Technol.*, *19*, 183–204, doi: 10.1175/1520-0426(2002).

Egbert, G. D., A. F. Bennett, and M. G. G. Foreman (1994), TOPEX/POSEIDON tides estimated using a global inverse model, *J. Geophys. Res.*, *99*, 24,821–24,852, doi:10.1029/94JC01894.

Fahrbach, E., J. Meincke, S. Østerhus, G. Rohardt, U. Schauer, V. Tverberg, and J. Verduin (2001), Direct measurements of volume transports through Fram Strait, *Polar Res.*, *20*, 217–224.

Fetterer, F., J. S. Stewart, and W. N. Meier (2015), *MASAM2: Daily 4-Km Arctic Sea Ice Concentration*, National Snow and Ice Data Center, Boulder, Colo., doi:http://dx.doi.org/10.7265/N5ZS2TFT. [Available at https://nsidc.org/data/docs/noaa/g10005-masam2/.]

Gomis, D., and M. A. Pedder (2005), Errors in dynamical fields inferred from oceanographic cruise data, *J. Mar. Syst.*, *56*, 317–333.

Hall, M. M. (1994), Synthesizing the Gulf Stream thermal structure from XBT data, *J. Phys. Oceanogr.*, *24*, 2278–2287, doi:10.1175/1520-0485.

Håvik et al. (2017), Evolution of the East Greenland current from Fram Strait to Denmark Strait: Synoptic measurements from summer 2012, *J. Geophys. Res. Oceans*, in press. [Available at http://onlinelibrary.wiley.com/doi/10.1002/2016JC012228/full.]

Ivanov, V. V., et al. (2009), Seasonal variability in Atlantic Water off Spitsbergen, *Deep Sea Res., Part I*, *56*, 1–14, doi:10.1016/j.dsr.2008.07.013.

Ivanov, V. V., V. A. Alexeev, I. Repina, N. V. Koldunov, and A. Smirnov (2012), Tracing Atlantic Water signature in the Arctic Sea ice cover east of Svalbard, *Adv. Meteorol.*, *2012*, 1–14, doi:10.1155/2012/201818.

Jakobsson, M., et al. (2012), The international bathymetric chart of the Arctic Ocean (IBCAO) version 3.0, *Geophys. Res. Lett.*, *39*, L12609, doi: 10.1029/2012GL052219.

Karcher, M., J. N. Smith, F. Kauker, R. Gerdes, and W. M. Smethie (2012), Recent changes in Arctic Ocean circulation revealed by iodine-129 observations and modeling, *J. Geophys. Res.*, *117*, C08007, doi:10.1029/2011JC007513.

Nansen, F. (1902), The oceanography of the North Polar Basin, in *The Norwegian North Polar Expedition 1893–1896: Science Results*, vol. 3, 427 pp., Longmans, Green, and Company, New York.

Onarheim, I. H., L. H. Smedsrud, R. B. Ingvaldsen, and F. Nilsen (2014), Loss of sea ice during winter north of Svalbard, *Tellus A*, *66*, 1–9.

Ou, H. W., and A. L. Gordon (1986), Spin-down of baroclinic eddies under sea ice, *J. Geophys. Res.*, *91*, 7623–7630, doi:10.1029/JC091iC06p07623.

Perkin, R. G., and E. L. Lewis (1984), Mixing in the West Spitsbergen current, *J. Phys. Oceanogr.*, *14*, 1315–1325.

Pickart, R. S. (1992), Space-time variability of the deep western boundary current oxygen core, *J. Phys. Oceanogr.*, *22*, 1047–1061.

Pickart, R. S, L. M. Schulze, G. W. K. Moore, M. A. Charette, K. Arrigo, G. van Dijken, and S. Danielson (2013), Long–term trends of upwelling and impacts on primary productivity in the Alaskan Beaufort Sea, *Deep Sea Res., Part I*, *79*, 106–121.

Pnyushkov, A. V., I. V. Polyakov, V. V. Ivanov, Y. Aksenov, A. C. Coward, M. Janout, and B. Rabe (2015), Structure and variability of the boundary current in the Eurasian Basin of the Arctic Ocean, *Deep Sea Res., Part I*, *101*, 80–97.

Polyakov, I. V., U. S. Bhatt, and H. L. Simmons (2005), Multidecadal variability of North Atlantic temperature and salinity during the twentieth century, *J. Geophys. Res.*, *18*, 4562–4581, doi:10.1175/JCLI3548.1.

Polyakov, I. V., et al. (2011), Fate of early 2000s Arctic warm water pulse, *Bull. Am. Meteorol. Soc.*, *92*, 561–566.

Randelhoff, A., and A. Sundfjord (2015), Seasonal variability and fluxes of nitrate in the surface waters over the Arctic shelf slope, *Geophys. Res. Lett.*, *42*, 3442–3449, doi:10.1002/2015GL063655.

Rudels, B. (1989), The formation of Polar Surface Water, the ice export and the exchanges through the Fram Strait, *Prog. Oceanogr.*, *22*, 205–248.

Rudels, B. (2013), Arctic Ocean circulation, processes and water masses: A description of observations and ideas with focus on the period prior to the International Polar Year 2007-2009, *Prog. Oceanogr.*, *132*, 22–67, doi:10.1016/j.pocean.2013.11.006.

Rudels, B., E. P. Jones, L. G. Anderson, and G. Kattner (1994), On the Intermediate Depth Waters of the Arctic Ocean, in *The Polar Oceans and Their Role in Shaping the Global Environment*, edited by O. M. Johannessen, R. D. Muench, and J. E. Overland, 14 pp., AGU, Washington, D. C., doi:10.1029/GM085p0033.

Rudels, B., et al. (2000), Water mass distribution in Fram Strait and over the Yermak Plateau in summer 1997, *Ann. Geophys.*, *18*, 687–705.

Rudels, B., E. P. Jones, U. Schauer, and P. Eriksson (2004), Atlantic sources of the Arctic Ocean surface and halocline waters, *Polar Res.*, *23*, 181–208.

Rudels, B., G. Björk, J. Nilsson, P. Winsor, I. Lake, and C. Nohr (2005), The interaction between waters from the Arctic Ocean and the Nordic Seas north of Fram Strait and along the East Greenland Current: Results from the Arctic Ocean-02 Oden expedition, *J. Mar. Syst.*, *55*, 1–30.

Rudels, B., U. Schauer, G. Björk, M. Korhonen, S. Pisarev, B. Rabe, and A. Wisotzki (2013), Observations of water masses and circulation in the Eurasian Basin of the Arctic Ocean from the 1990s to the late 2000s, *Ocean Sci.*, *9*, 147–169.

Rudels, B., M. Korhonen, U. Schauer, S. Pisarev, B. Rabe, and A. Wisotzki (2015), Circulation and transformation of Atlantic water in the Eurasian Basin and the contribution of the Fram Strait inflow branch to the Arctic Ocean heat budget, *Prog. Oceanogr.*, *132*, 128–152.

Saloranta, T. M., and P. M. Haugan (2001), Interannual variability in the hydrography of Atlantic water northwest of Svalbard, *J. Geophys. Res.*, *106*, 13,931–13,943.

Schauer, U., and A. Beszczynska-Möller (2009), Problems with estimation and interpretation of oceanic heat transport—Conceptual remarks for the case of Fram Strait in the Arctic Ocean, *Ocean Sci.*, *5*, 487–494.

Schauer, U., R. D. Muench, B. Rudels, and L. Timokhov (1997), Impact of eastern Arctic shelf waters on the Nansen Basin intermediate layers, *J. Geophys. Res.*, *102*, 3371–3382.

Schauer, U., et al. (2002), Confluence and redistribution of Atlantic water in the Nansen, Amundsen and Makarov basins, *Ann. Geophys.*, *20*, 257–273.

Schauer, U., E. Fahrbach, S. Østerhus, and G. Rohardt (2004), Arctic warming through the Fram Strait: Oceanic heat transport from 3 years of measurements, *J. Geophys. Res.*, *109*, C06026, doi:10.1029/2003JC001823.

Smedsrud, L. H., R. Ingvaldsen, J. E. Ø. Nilsen, and Ø. Skagseth (2010), Heat in the Barents Sea: Transport, storage, and surface fluxes, *Ocean Sci.*, *6*, 219–234, doi:10.5194/os-6-219-2010.

Spall, M. A. (1995), Frontogenesis, subduction, and cross-front exchange at upper ocean fronts, *J. Geophys. Res.*, *100*, 2543–2557, doi:10.1029/94JC02860.

Spall, M. A., R. S. Pickart, P. S. Fratantoni, and A. J. Plueddemann (2008), Western Arctic shelfbreak eddies: Formation and transport, *J. Phys. Oceanogr.*, *38*, 1644–1668.

Teigen, S. H., F. Nilsen, R. Skogseth, B. Gjevik, and A. Beszczynska-Möller (2011), Baroclinic instability in the West Spitsbergen Current, *J. Geophys. Res.*, *116*, C07012, doi:10.1029/2011JC006974.

Tsubouchi, T., et al. (2012), The Arctic Ocean in summer: A quasi-synoptic inverse estimate of boundary fluxes and water mass transformation, *J. Geophys. Res.*, *117*, C01024, doi:10.1029/2011JC007174.

Våge, K., R. S. Pickart, V. Pavlov, P. Lin, D. J. Torres, I. Ingvalsen, A. Sundjord, and A. Proshutinsky (2016), The Atlantic Water boundary current in the Nansen Basin east of Fram Strait, *J. Geophys. Res. Oceans*, doi:10.1002/2016JC011715, in press.

Walczowski, W., and J. Piechura (2011), Influence of the West Spitsbergen Current on the local climate, *Int. J. Climatol.*, *31*, 1088–1093.

Woodgate, R. A., K. Aagaard, R. D. Muench, J. Gunn, G. Björk, B. Rudels, A. T. Roach, and U. Schauer (2001), The Arctic Ocean boundary current along the Eurasian slope and the adjacent Lomonosov Ridge: Water mass properties, transports and transformations from moored instruments, *Deep Sea Res., Part I*, *48*, 1757–1792.

Woodgate, R. A., K. Aagaard, J. H. Swift, W. M. Smethie, and K. K. Falkner (2007), Atlantic water circulation over the Mendeleev Ridge and Chukchi Borderland from thermohaline intrusions and water mass properties, *J. Geophys. Res.*, *112*, C02005, doi:10.1029/2005JC003416.